Electronic Supporting Information

Tuning the Electrical Conductance of Oligo(phenylene-ethynylene) Derivatives-PbS Quantum-dot Bilayers

Ali Ismael,[a,b*,†] Xintai Wang,[c,d,e*,†] Alaa Al-Jobory,[a,f,†] Shanglong Ning,[d,†] Turki Alotaibi,[a,g†] Bashayr Alanazi,[a,h] Hanan Althobaiti,[a,i] Junsheng Wang,[c] Christopher J. B. Ford[d*] and Colin J. Lambert[a*]

Contents

1. DFT and Transport Simulations

In this section, geometries, electronic structures and transport properties of all junctions are presented. The main aim in this study is to examine the change in transport properties when a PbS quantum dot is inserted in a Gr-Au junction for three different molecules.

1.1 Optimised DFT Structures of Isolated Molecular-scale Structures

Using the density-functional code SIESTA[1], the optimum geometries of the isolated molecules were obtained by relaxing the molecules until all forces on the atoms were less than 0.01 eV/Å. A double-zeta plus polarization orbital basis set, norm-conserving pseudopotentials, and energy cut-off of 250 Rydbergs defining the real-space grid were used and the local-density approximation (GGA)[2-4] was chosen as the exchange-correlation functional. The basic building blocks I-IV of this study are shown in Fig. S1. The PbS quantum dot is a truncated octahedron, or a polyhedron with 14 faces, and Fig. S2 illustrates the 8 hexagonal faces from different angles.

1   **2**

3   **PbS nanoparticle**

Figure S1: Simulated structures: molecules **1−3**, and the PbS quantum dot. Key: C = grey, H = white, O = red, S = yellow, N=blue, Pb = dark grey.

Figure S2: Structure of the PbS truncated octahedron viewed from different angles[5]. Key: S = yellow, and Pb = dark grey.

The molecular structures were assembled by combining the above molecules 1−3 of Figs. 1 and S1 with the PbS quantum dot, and then allowing the system to become fully relaxed, to yield the structures such as those shown in Fig. S3.
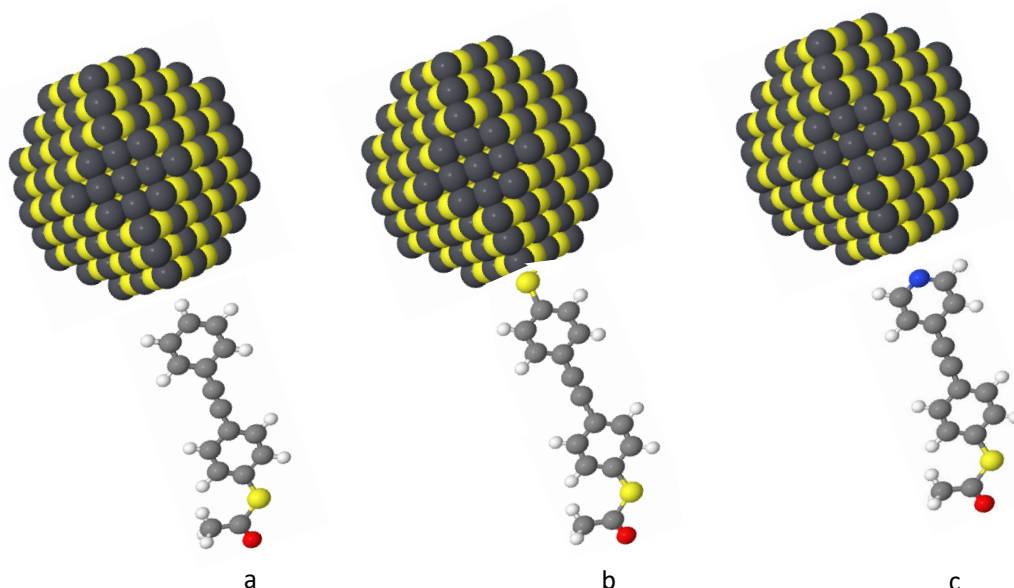
Figure S3: Schematic illustrations of isolated molecules **1-3** attached to the PbS quantum dot to form molecule/quantum-dot bilayer. **a:** molecule **1** + PbS, **b:** molecule **2** + PbS, **c:** molecule **3** + PbS. Key: grey: C, white: H, blue: N, dark grey: Pb, yellow: S, red: O.

1.2 Frontier molecular orbitals

As a first step towards understanding their electronic properties, the frontier orbitals of the studied molecules were computed, including the highest occupied molecular orbital (HOMO), lowest unoccupied orbital (LUMO), in addition to their HOMO+1, and LUMO−1, along with their orbital energies. Frontier orbitals of the isolated PbS quantum dot are shown in Fig. S4, and those of the quantum dot with a graphene sheet are shown in Fig. S5, followed by the frontier orbitals of the quantum dot with the graphene sheet plus molecule **1** (Fig. S6), **2** (Fig. S7), and **3** (Fig. S8). The green and yellow colours represent the positive and negative orbital amplitudes.

1.2.1 PbS quantum dot

E_F = -3.28 eV

HOMO = −4.82 eV

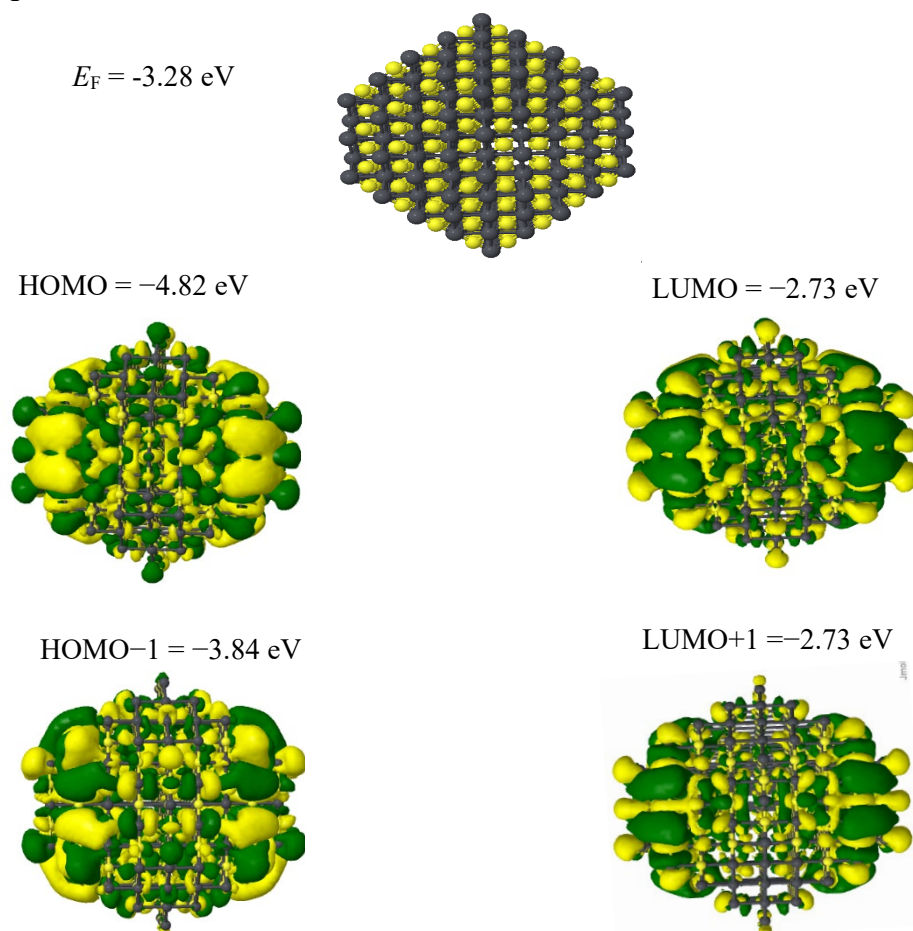LUMO = −2.73 eV

HOMO−1 = −3.84 eV

LUMO+1 =−2.73 eV

Figure S4: Frontier orbitals of the isolated truncated octahedron PbS quantum dot. Top panel: fully optimised geometry of the dot. Lower panel: HOMO, LUMO, HOMO–1, LUMO+1 of the PbS quantum dot, along with their energies.
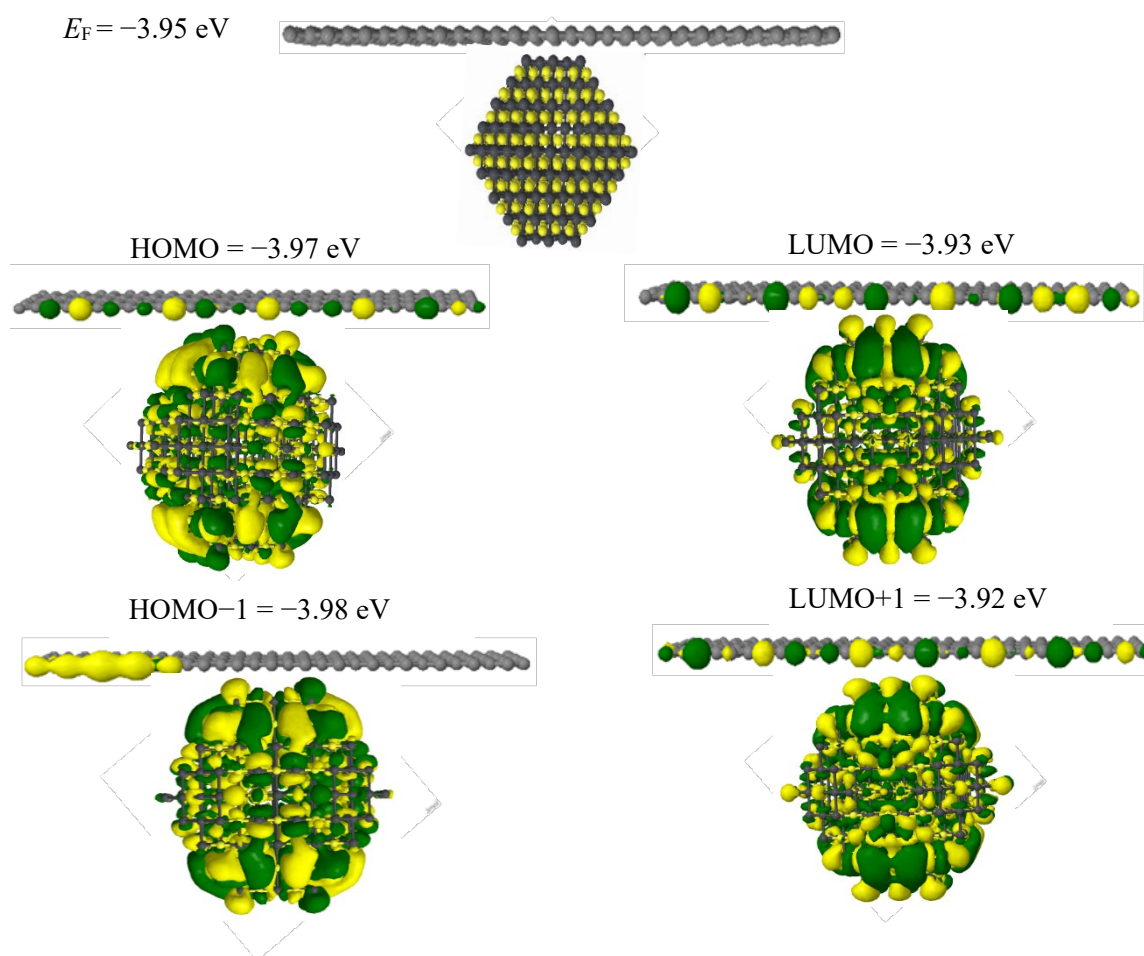
1.2.2 PbS quantum dot + Gr sheet

$E_F = -3.95$ eV

HOMO = −3.97 eV   LUMO = −3.93 eV

HOMO−1 = −3.98 eV   LUMO+1 = −3.92 eV

Figure S5: Frontier orbitals of a PbS quantum dot + Gr sheet. Top panel: fully optimised geometry of PbS quantum dot + Gr sheet. Lower panel: HOMO, LUMO, HOMO–1, LUMO+1.

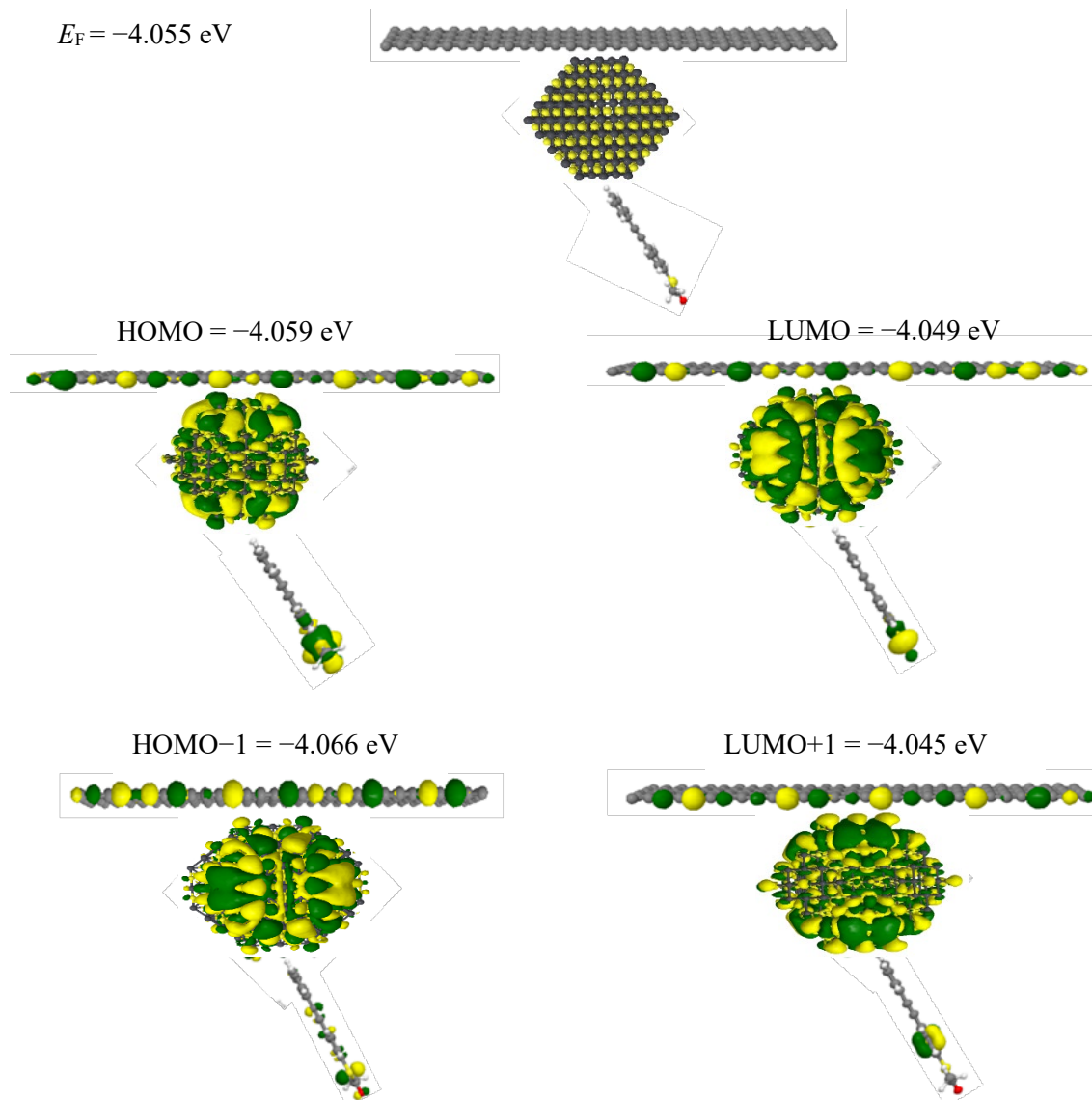### 1.2.3 PbS quantum dot + Gr sheet + Molecule 1

$E_F = -4.055$ eV

HOMO = -4.059 eV

LUMO = -4.049 eV

HOMO-1 = -4.066 eV
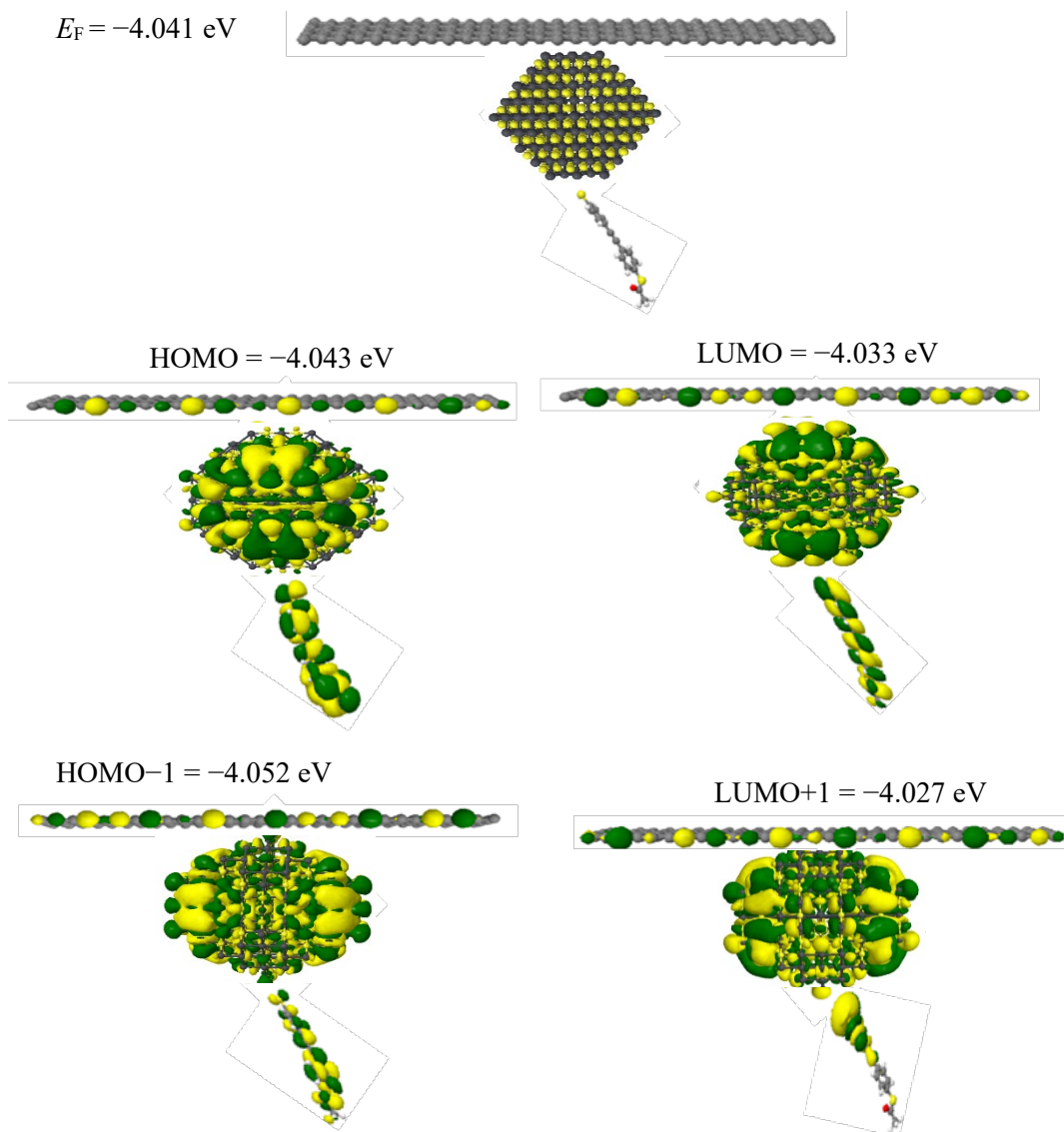
LUMO+1 = -4.045 eV

Figure S6: Frontier orbitals of a PbS quantum dot + Gr sheet + molecule **1**. Top panel: fully optimised geometry of PbS quantum dot + Gr sheet + molecule **1**. Lower panel: The corresponding HOMO, LUMO, HOMO–1, LUMO+1 along with their energies.

1.2.4 PbS quantum dot + Gr sheet + Molecule 2

$E_F = -4.041$ eV

HOMO = −4.043 eV

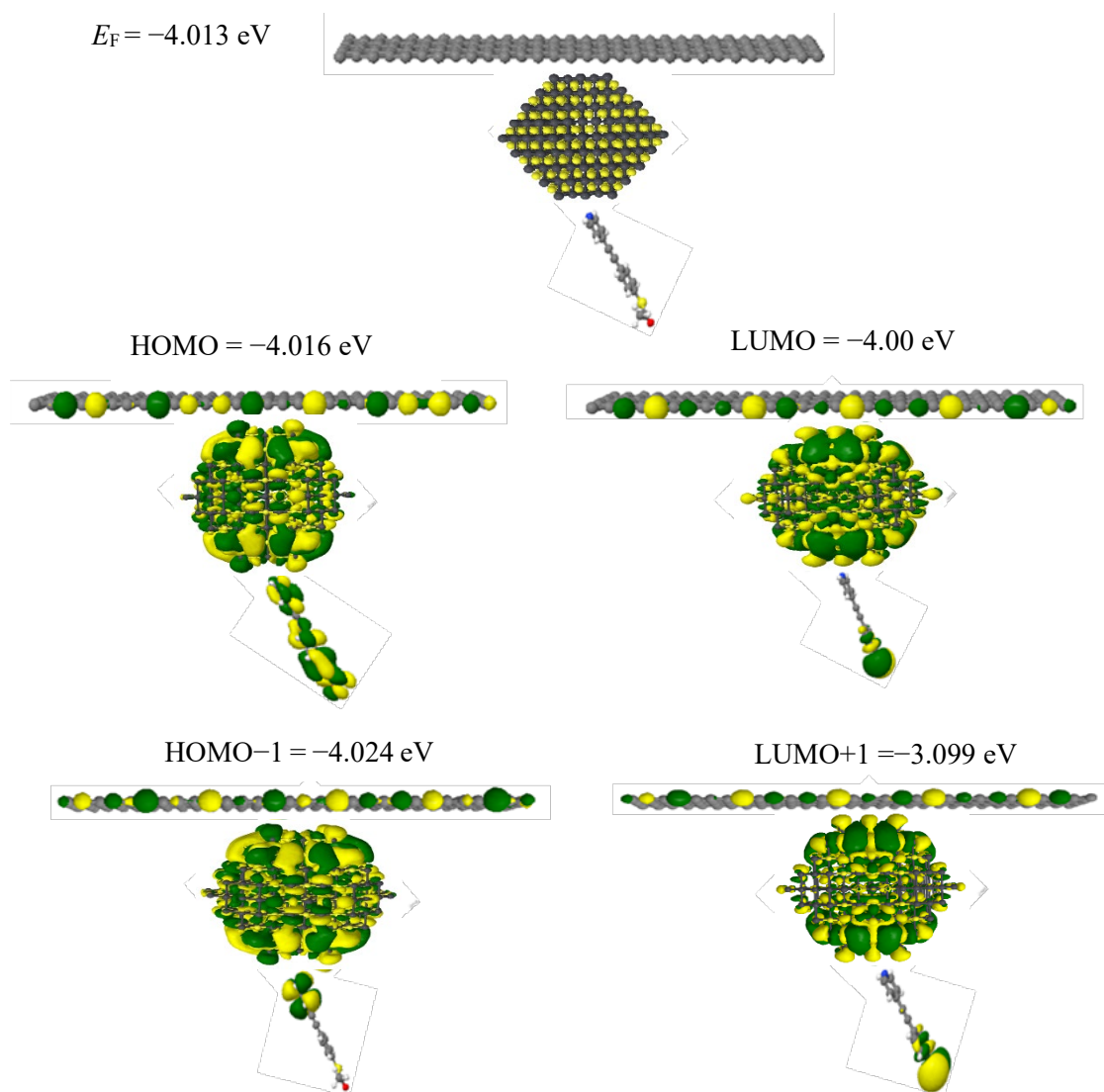LUMO = −4.033 eV

HOMO−1 = −4.052 eV

LUMO+1 = −4.027 eV

Figure S7: Frontier orbitals of a PbS quantum dot + Gr sheet + molecule **2**. Top panel: fully optimised geometry of PbS quantum dot + Gr sheet + molecule **2**. Lower panel: The corresponding HOMO, LUMO, HOMO–1, LUMO+1 along with their energies.

1.2.4 PbS quantum dot + Gr sheet + Molecule 3

$E_F = -4.013$ eV

HOMO = −4.016 eV

LUMO = −4.00 eV

HOMO−1 = −4.024 eV

LUMO+1 = −3.099 eV

Figure S8: Frontier orbitals of a PbS quantum dot + Gr sheet + molecule **3**. Top panel: fully optimised geometry of PbS quantum dot + Gr sheet + molecule **3**. Lower panel: The corresponding HOMO, LUMO, HOMO–1, LUMO+1 along with their energies.

1.3 Binding energies

To calculate the optimum binding distance between any two entities labelled A and B, we use DFT and the counterpoise method, which removes basis-set superposition errors (BSSE). The binding distance d is defined as the optimum distance between A and B, which minimises their total energy. The ground-state energy of the total system is calculated using SIESTA and is denoted E_{AB}^{AB}. The energy of each entity is then calculated in a fixed basis, which is achieved using ghost atoms in SIESTA. Hence, the energy of A in the presence of the fixed basis is defined as E_{A}^{AB} and for B as E_{B}^{AB}. The binding energy is then calculated using the following equation[6-8]:

$$\text{Binding Energy} = E_{AB}^{AB} - E_{A}^{AB} - E_{B}^{AB} \qquad (S1)$$

1.3.1 Binding energy of two components (PbS and Gr sheet)

In this section, the optimum distance between the PbS quantum dot and graphene sheet is calculated to be between 4.1 and 4.2 Å, and their binding energy is approximately –0.18 eV. Results are shown for two different orientations, corresponding to a pure Pb facet binding to the graphene surface (black curve in Fig. S9) and a mixed (Pb + S) facet (red curve in Fig. S9).
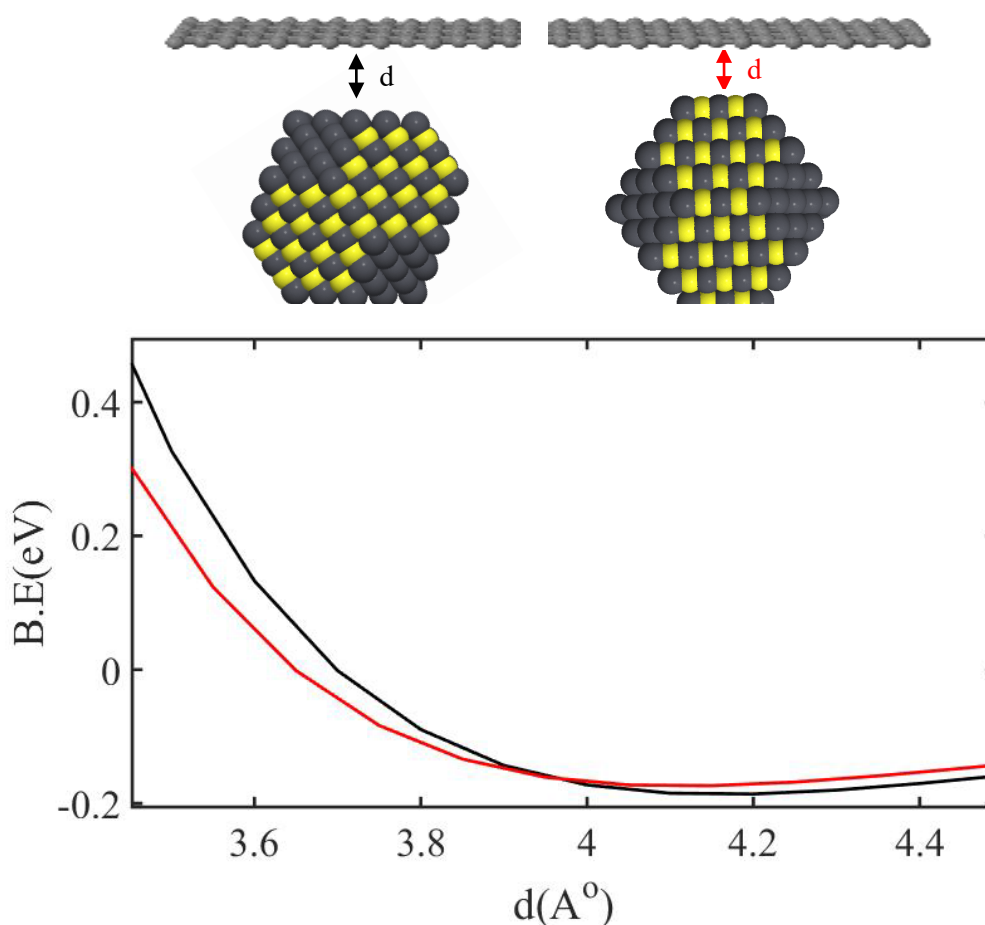
Figure S9: Top panel: Representation of the PbS quantum dot binding to a graphene sheet. Lower panel: Binding energy as a function of the binding distance d, where the optimum d is found to be approximately between 4.1 and 4.2 Å.

1.3.2 Binding energy of two components (molecule 1 and PbS)

Figure S10 shows the binding energy between the phenyl ring of molecule **1** and a S atom of the PbS quantum dot. The optimum binding distance d is found to be 2.9 Å, corresponding to a binding energy of 0.0035 eV. Similarly, Fig. S11 shows the binding energy between the phenyl ring of molecule 1 and a Pb atom of the PbS quantum dot, which is found to be around 0.0046 eV. These weak binding energies suggest that the PbS quantum dot does not bind to the phenyl group of molecule **1**. Therefore, we do not consider this scenario (molecule **1** + PbS quantum dot) further and we restrict the following study to molecules **2** and **3** combined with a PbS quantum dot.
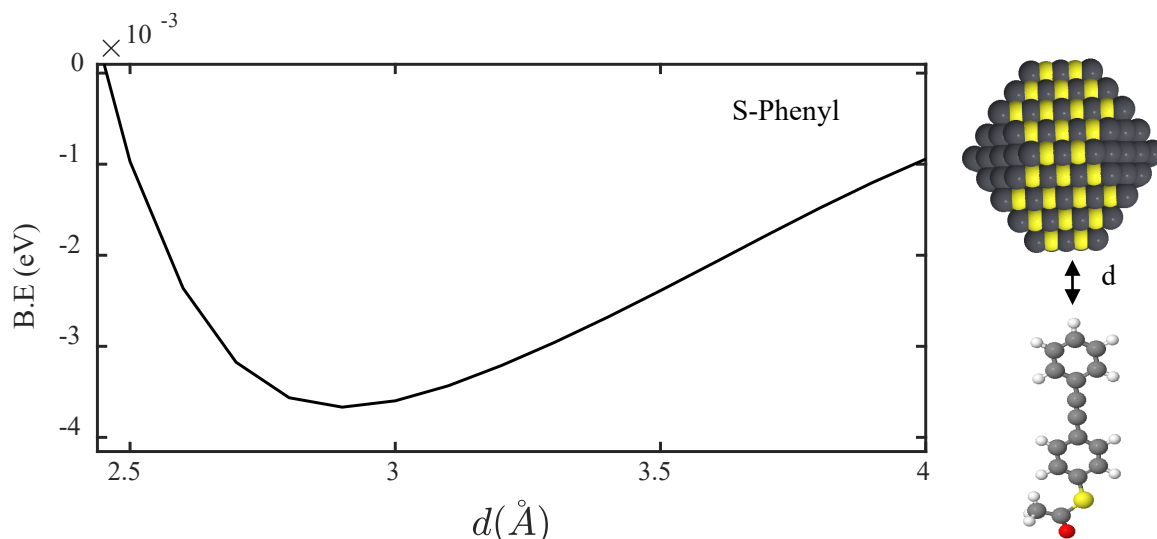
Figure S10: Right panel: representation of the PbS quantum dot binding to molecule **1** through a S atom. Left panel: Binding energy as a function of the binding distance d, where the optimum d is found to be approximately 2.9 Å, and binding energy B.E. = 0.0035 eV.
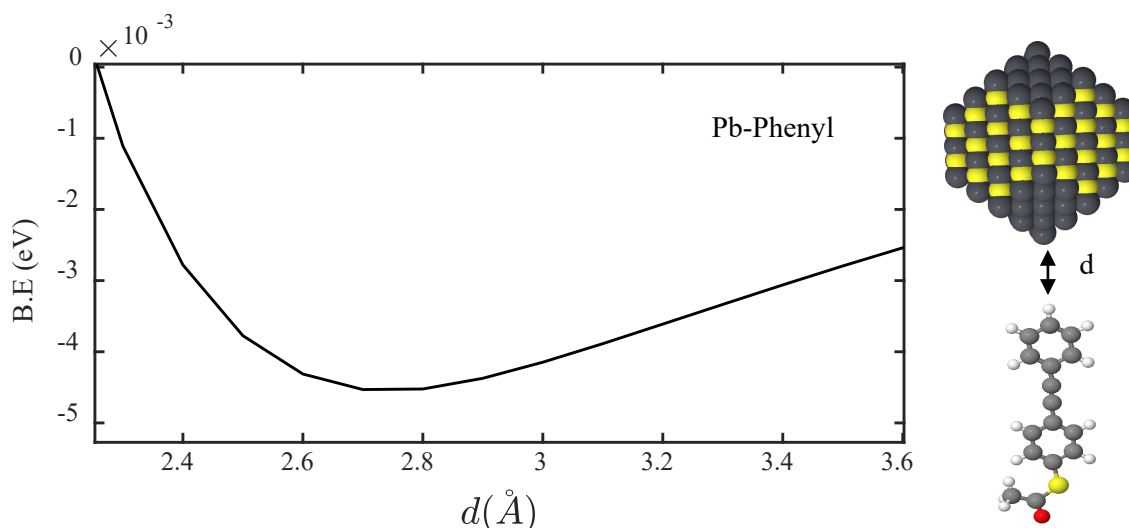

Figure S11: Right panel: The PbS quantum dot binding to molecule **1** through a Pb atom. Left panel: Binding energy as a function of the binding distance d, where the optimum d is found to be approximately 2.7 Å, and binding energy B.E. = 0.0045 eV.

1.3.3 Binding energy of two components (molecule 2 and PbS)

Figure S12 shows the binding energy between molecule 2 and the PbS quantum dot, with the thiol group binding to a S atom of the PbS. The optimum binding distance d is found to be 2.2 Å, at a binding energy of approximately 0.10 eV. Fig. S13 shows the binding energy between molecule **2** and the PbS quantum dot, with the thiol binding to a Pb atom of the PbS. The optimum d is 3.2 Å, with B.E. $\approx$ 0.54 eV. These high binding energies show that the PbS quantum dot also binds strongly to the thiol of molecule **3**.
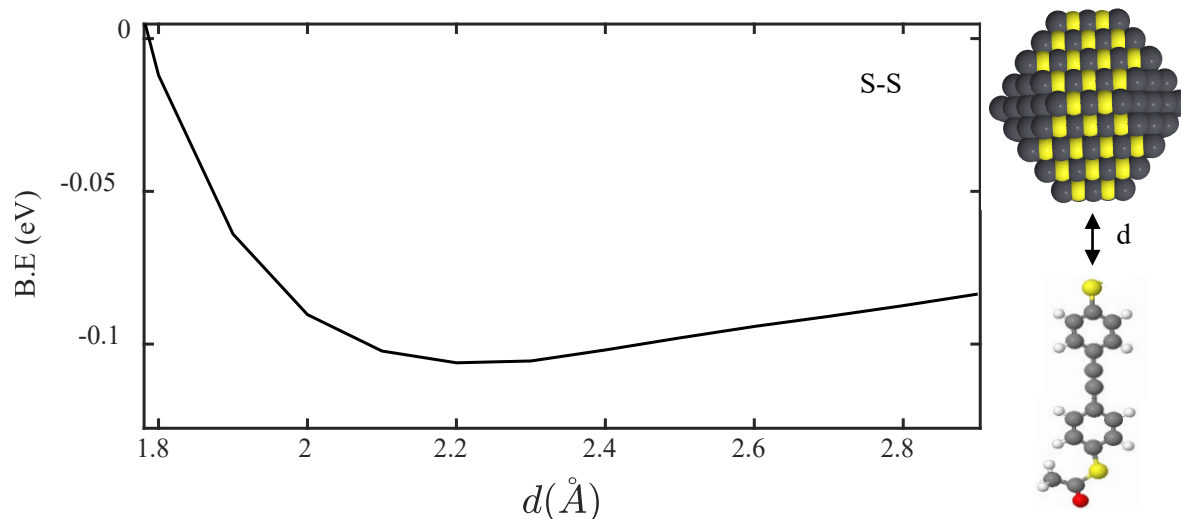
Figure S12: Right panel: The PbS quantum dot binding to molecule **2** through a S atom. Left panel: Binding energy as a function of the binding distance d, where the optimum d is found to be approximately 2.2 Å, and binding energy B.E. = 0.10 eV.
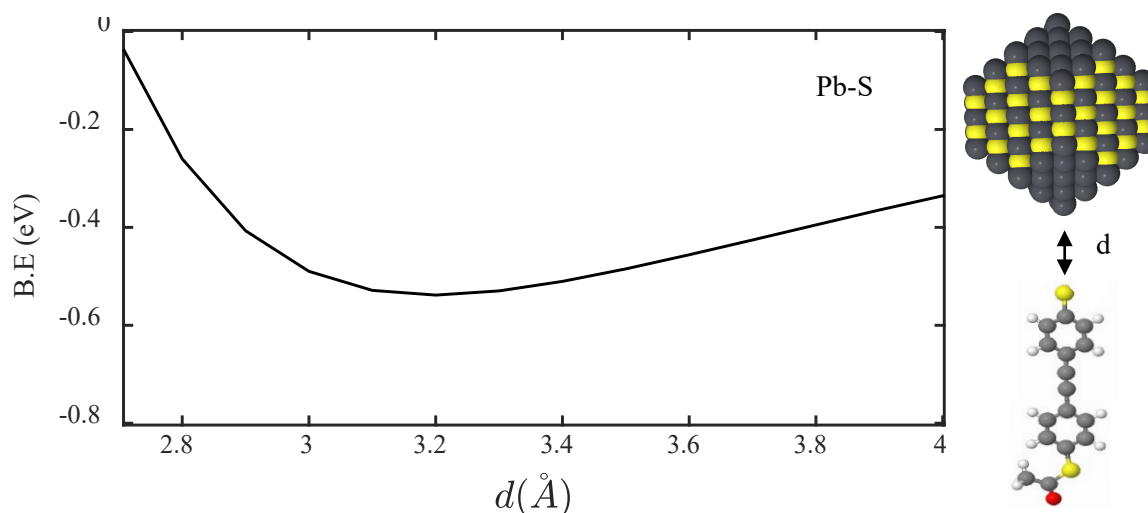

Figure S13: The PbS quantum dot binding to molecule **2** through Pb atom. Left panel: Binding energy as a function of the binding distance d, where the optimum d is found to be approximately 3.2 Å, and binding energy B.E. = 0.54 eV.

1.3.4 Binding energy of molecule 3 and PbS

Figure S14 shows the binding energy between molecule **3** and the PbS quantum dot, with the pyridyl group binding to a S atom of the PbS. The optimum binding distance d is found to be 3.9 Å, at a binding energy of approximately 0.012 eV. Fig. S15 shows the binding energy between molecule **2** and the PbS quantum dot, with the pyridyl group binding to a Pb atom of the PbS. The optimum d is 3.4 Å, with B.E. ≈ 0.38 eV. These high binding energies show that the PbS quantum dot binds strongly to the pyridyl group of molecule **3**.
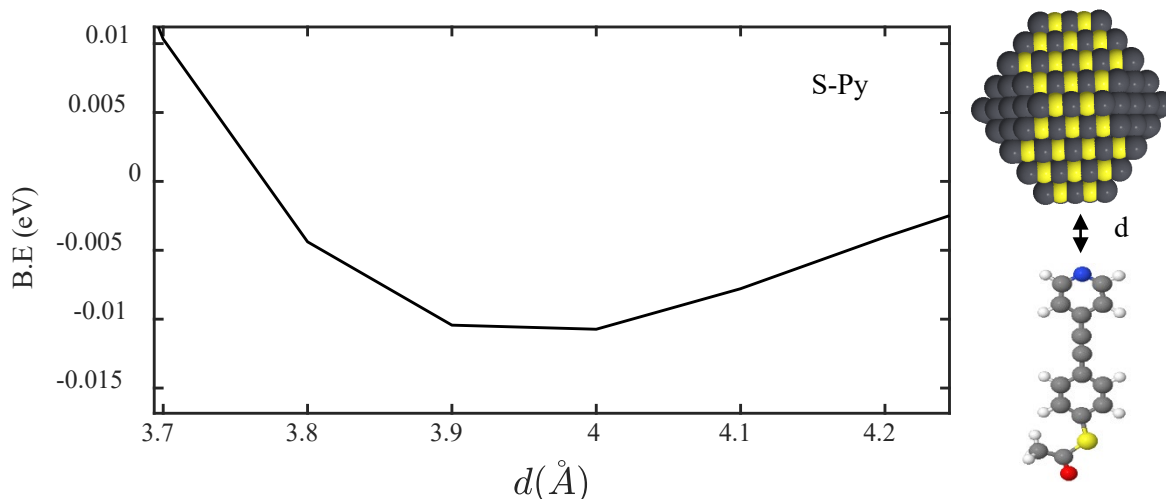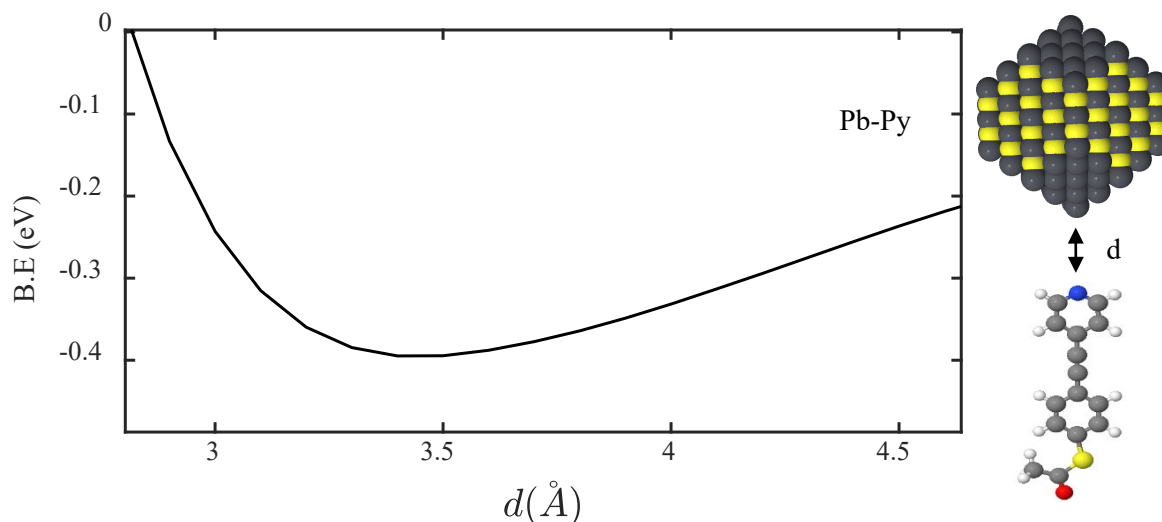
Figure S14: Right panel: The PbS quantum dot binding to molecule **2** through a S atom. Left panel: Binding energy as a function of the binding distance d, where the optimum d is found to be approximately 3.9 Å and the binding energy B.E. = 0.012 eV.

Figure S15: Right panel: The PbS quantum dot binding to molecule **2** through a Pb atom. Left panel: Binding energy as a function of the binding distance d. The optimum d is found to be approximately 3.4 Å, and binding energy B.E. = 0.38 eV.

Molecule	Contact point (PbS quantum dot)	Optimum d (Å)	B.E. (eV)
	S	2.9	0.0035
1	Pb	2.7	0.0045
	S	2.2	0.099
2	Pb	3.2	0.540
	S	3.9	0.012
3	Pb	3.4	0.380

Table S1: Binding energies (B.E.) and optimum distances d predicted for the three molecules in contact with a PbS quantum dot through two different contact points (S or Pb).

Table S1 demonstrates that molecule **1** does not bind to the PbS quantum dot neither via a S or a Pb atom, because the binding energies are smaller than k_BT at room temperature (at which $k_BT = 0.025$ eV). Similarly, molecule **2** will not bind to a S atom of the quantum dot, while molecule **3** will bind only weakly to it. In contrast, both molecules **2** and **3** show significant binding to a Pb atom of the quantum dot.

1.4 Optimised DFT structures of junctions in the presence of single-layer graphene (SLG)

Using the optimised structures and geometries for the compounds obtained as described above, we again employed the SIESTA code to calculate self-consistent optimised geometries, ground-state Hamiltonians and overlap matrix elements for each graphene-molecule-gold junction. This section includes two asymmetric and one symmetric molecule with different anchor groups including phenyl ring, pyridyl and thiol. These molecules sandwiched between gold and single-layer graphene sheet (SLG), and for this purpose we shall explore three different junctions a, b and c as shown in Fig. S16.

The binding energy calculations above demonstrate that the phenyl ring of molecule **1** does not bind to the PbS quantum dot, unlike the pyridyl and thiol anchors (molecules **2** and **3** respectively). Therefore, in the experiments, after washing, the PbS quantum dot is no longer present, resulting in the Au-**1**-SLG junction shown in Fig. 16a.
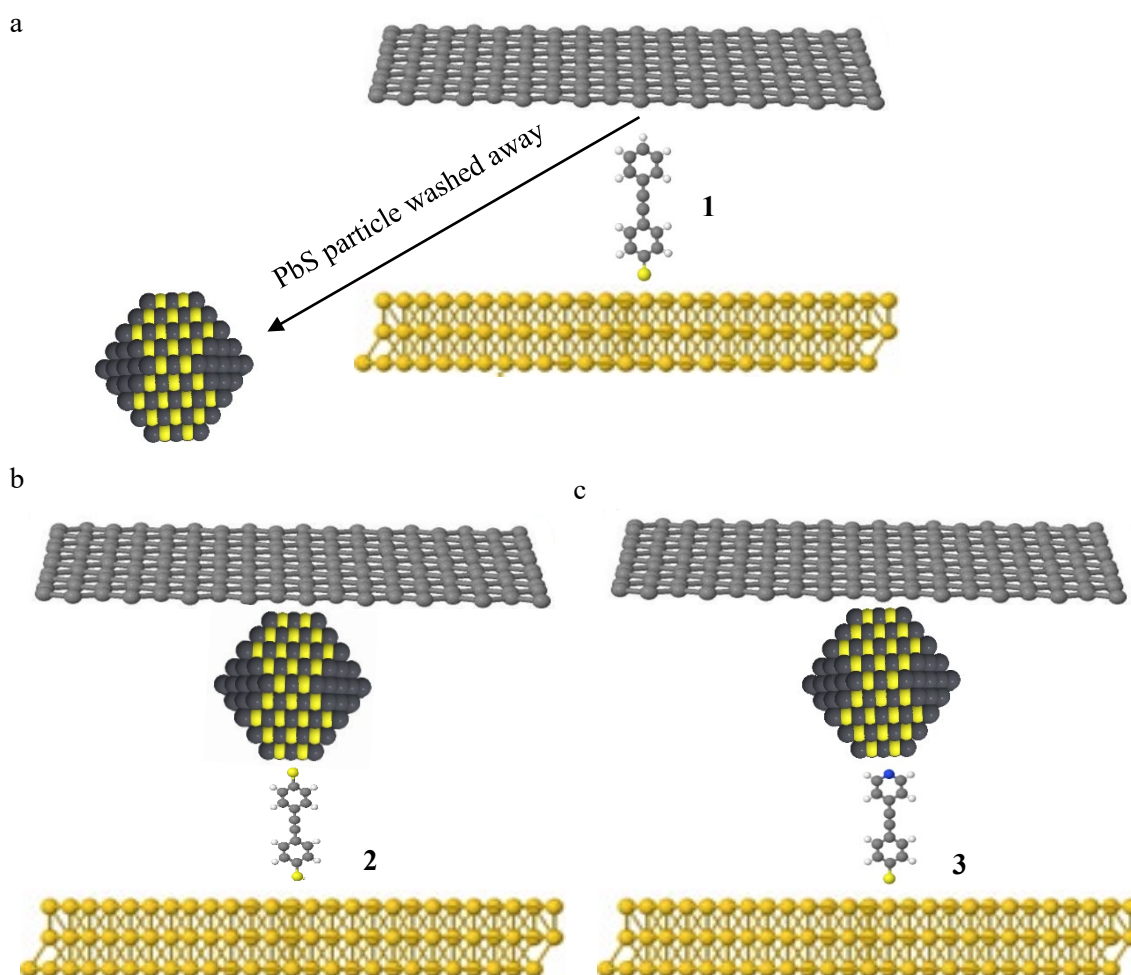

Figure S16: Schematic illustration of the Au/**1-3**/SLG junctions. Top contact is a SLG electrode and the bottom contact is a Au electrode. **a:** Au/**1**/SLG junction, the PbS quantum dot is washed away due to weak binding between the phenyl ring and PbS. **b:** Au-**2+PbS**-SLG junction. **c:** Au-**3+PbS**-SLG junction.

1.5 Quantum-dot contacting possibilities

Since the PbS quantum dot is a truncated octahedron, there are several potential contact points between the PbS and a molecule, as shown in Fig. S17. The PbS possesses 14 faces: 8 regular hexagons and 6 squares and we shall investigate these. The surfaces of four of the square facets contain Pb atoms only (sq. 1−4, black), and two are a mixture of Pb and S atoms (sq. 5−6, red). In contrast, all of the 8 hexagons are a mixture of S and Pb atoms (hex. 1−8, black and red), as shown in Fig. S17b. (Grey and yellow colours represent Pb and S atoms respectively.) Combining the PbS quantum dot with the molecule at the 14 faces form yields the molecule-quantum dot bilayers explored in the next section.
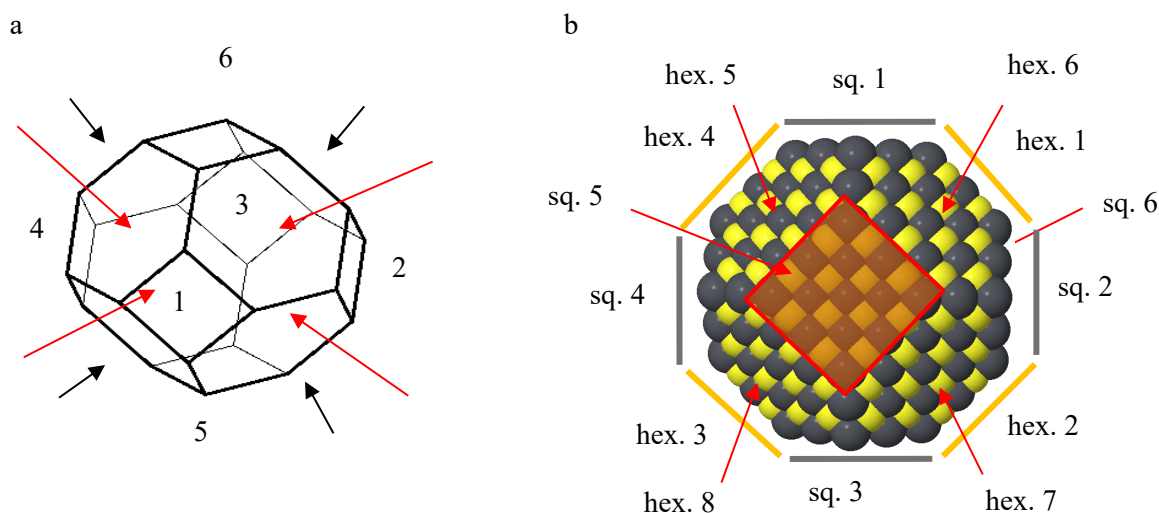

Figure S17: Schematic illustration of the PbS quantum dot showing some possible contact faces. **a:** Schematic illustration of truncated octahedron illustrating examples of the 14 faces comprising 6 squares and 8 hexagons (numbers and arrows in colours). **b:** The same PbS quantum dot with Pb and S atoms, with grey and yellow colours representing Pb and S atoms respectively.

1.6 Transport simulation in Au-molecule-SLG and Au-molecule-quantum dot-SLG Junctions

In the following transport calculations, the ground-state Hamiltonian and optimized geometry of each compound were again obtained using the density functional theory (DFT) code. The local density approximation (GGA) exchange correlation functional was used along with double zeta polarized (DZP) basis sets and the norm conserving pseudo potentials. The real space grid was defined by a plane wave cut-off of 250 Ry. The geometry optimisation was carried out to a force tolerance of 0.01 eV/Å. This process was repeated for a unit cell with the molecule between graphene and gold electrodes where the optimised distances between SLG-Au and the anchor groups are shown in Table S1. From the ground-state Hamiltonian, the transmission coefficient, the room-temperature electrical conductance G was obtained, as described in the subsections below. In this section, the bi-component is formed by combining the molecules 1−3, with PbS quantum dot through either S or Pb atoms and as follows.

1.6.1 Au-1-SLG junction

Based on the binding-energy simulations (see Table S1), the quantum dot is washed away from this junction and the junction measured experimentally is therefore a Au/1/SLG junction. The calculated transmission coefficient $T(E)$ for this junction is shown in the lower panel of Fig. S18. It should be noted that molecule 1 possesses only one orientation in the junction, because the thiol binds stronger to the gold than graphene as reported in ref. 9.
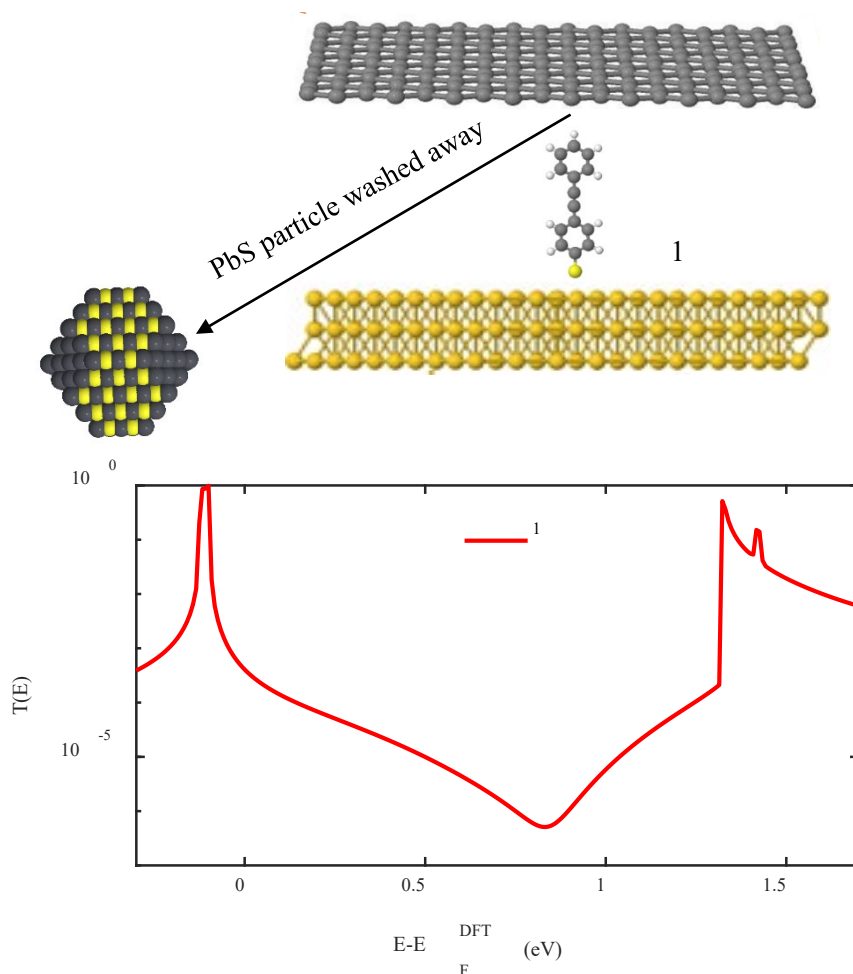
Figure S18: Top panel: Schematic illustration of the Au-**1**-SLG junction. Top contact is a SLG electrode and the bottom contact is a Au electrode. The PbS quantum dot is washed away due to the weak binding between the phenyl ring and PbS (0.003 eV). Lower panel: Zero-bias transmission coefficient $T(E)$ of a Au-**1**-SLG junction (this result reported in ref. 9).

1.6.2 Au-2-quantum dot-SLG junctions

The frontier molecular orbital plots presented in section 1.2 suggest that the PbS quantum dot possesses more weight on the faces, which explains why the molecule binds to the central atom of each face. The binding-energy simulation suggests that the PbS quantum dot can bind to Pb and S atoms, although binding to a Pb atom is favoured. Taking into account these parameters, we investigate the transmission coefficient for 14 different junctions and as follows: 6 through square faces: sq. 1−6 (Fig. S19b), and 8 through hexagonal faces: hex. 1−8 (Fig. S20b).
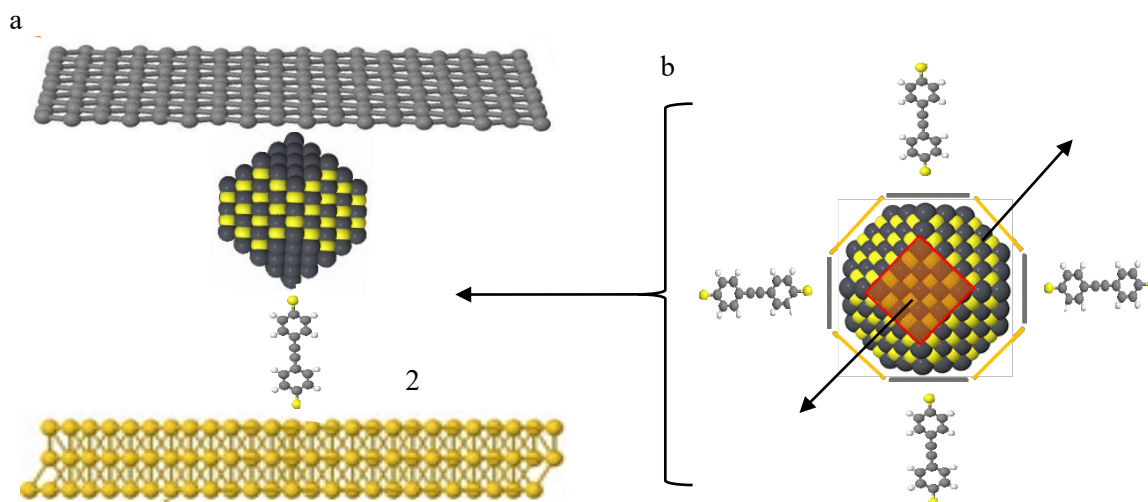
Figure S19: **a:** Schematic illustration of the Au-**2**-PbS-SLG junction. **b:** Six different contacts through square faces (sq. 1−6), to form the bilayer (**2** + PbS). Note: only four bilayers are shown and the other two are represented by black arrows.
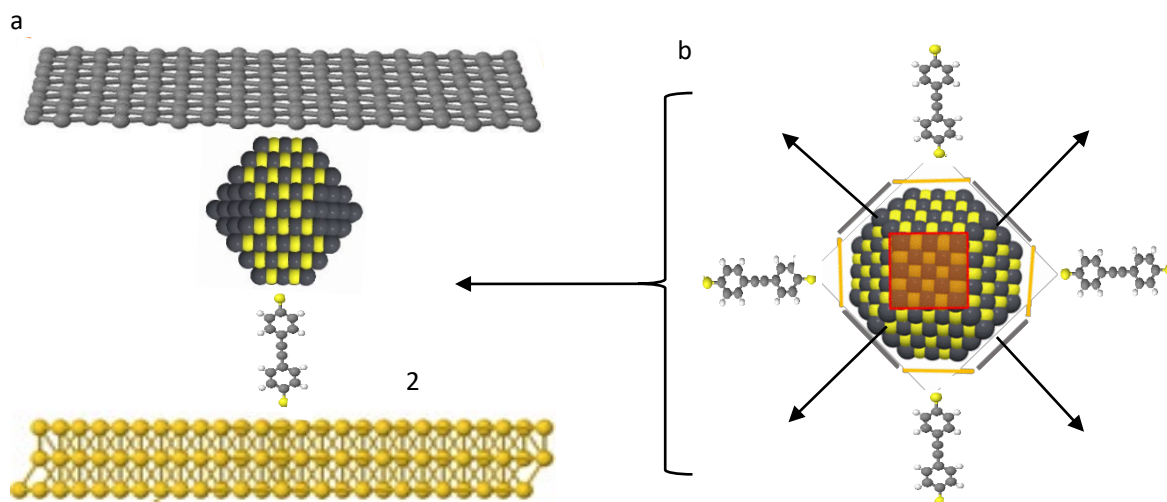

Figure S20: **a:** Schematic illustration of the Au-**2**-PbS-SLG junction. **b:** Eight different contacts through hexagonal faces (hex. 1−8), to form the bilayer (**2** + PbS). Note: only four bilayers are shown and the other four are represented by black arrows.

Figure S21 shows the transmission coefficients of the bilayer 2 (molecule **2** + PbS quantum dot), and the bilayer sandwiched between Au and SLG. The six curves correspond to the cases when molecule **2** attach to six faces of the PbS particle through square faces: sq. 1−6 (Fig. 19b). The four pristine Pb faces yield small differences in the conductance as shown by the grey curves and that is expected, as the four faces are identical. Regarding the two mixed square faces (Pb and S), the conductance is slightly higher, as shown by the two black curves.

We now consider the case where molecule **2** is attached to the eight identical hexagonal faces of the PbS quantum dot. Transmission curves are computed for eight different attachments: four of them attach the pyridyl to four S atoms of the hexagon and four to Pb atoms of the hexagon, as illustrated in Fig. 20b. The eight hexagon faces yield slightly higher differences in the conductance, as shown by the orange and grey curves of Fig. S22 (S and Pb respectively). Comparison between Fig. S21 and Fig. S22 shows that attachment to the different atoms of hexagonal facets yields a broader distribution of transmission coefficients than attachment to the various atoms of square facets.
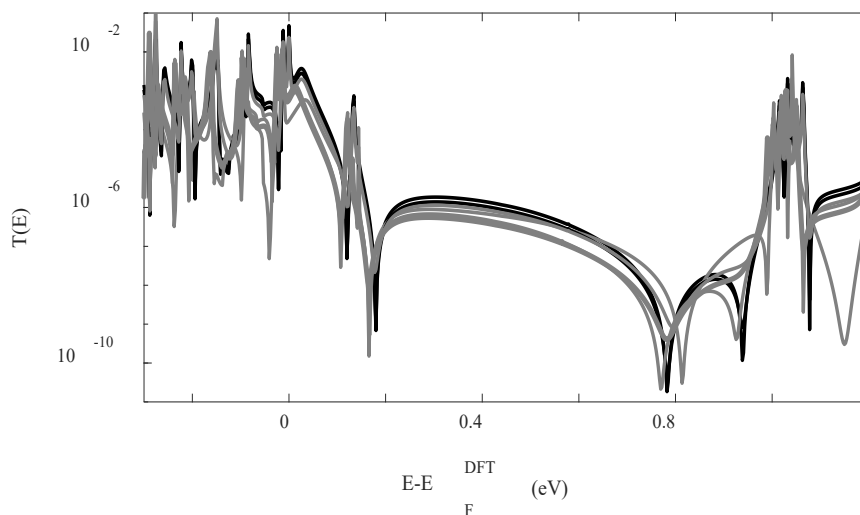
Figure S21: Zero-bias transmission coefficient *T*(*E*) of Au-**2-PbS**-SLG junctions *vs* electron energy *E*. The bilayer (**2** + PbS) is formed where the molecule **2** bilayer connects to the quantum dot via square faces: grey curves are for pure Pb atoms at the surface while black curves are for a mixture of S and Pb atoms.
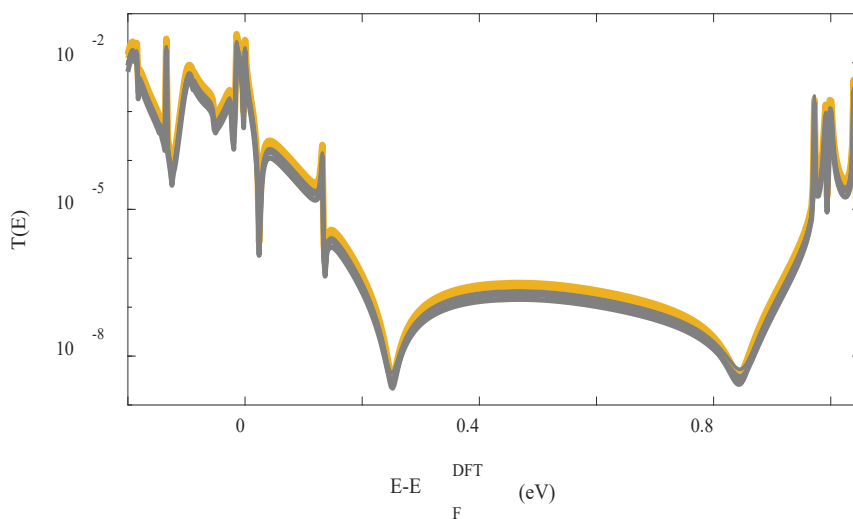

Figure S22: Zero-bias transmission coefficient *T*(*E*) curves of Au-**2-PbS**-SLG junctions *vs* electron energy *E*. The bilayer (**2** + PbS) is formed where the molecule **2** bilayer connects to the quantum dot via hexagonal faces: orange curves are where the molecule attaches to S atoms at the surface while grey curves are for attachment to Pb atoms.
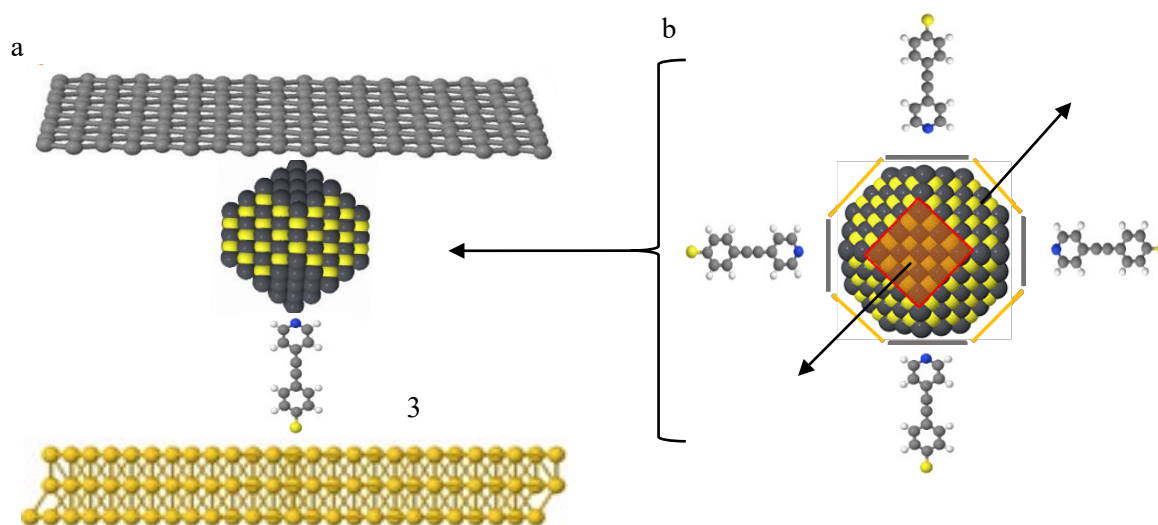
1.6.2 Au-3-quantum dot-SLG junctions

Figure S23: **a:** Schematic illustration of a Au-**3**-PbS-SLG junction. **b:** Six different contacts through square faces (sq. 1−6) to form the bilayer (**3**-PbS). (Only four bilayers are shown and the other two are indicated by black arrows.)

The 14 junctions of bilayer **2** are: six square faces (sq. 1−6) (Fig. S23b), and eight hexagonal faces (hex. 1−8) (Fig. S24b).
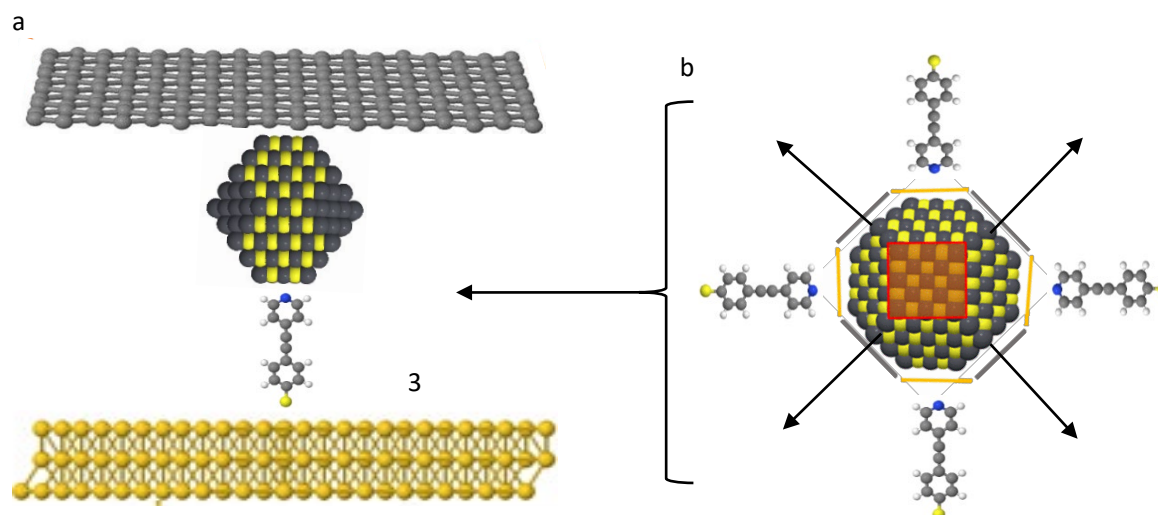

Figure S24: **a:** Schematic illustration of the Au-**3**-PbS-SLG junction. **b:** Eight different contacts through hexagon faces (hex. 1−8), to form the bilayer (**3**-PbS). (Only four bilayers are shown and the other four are indicated by black arrows.)

The same approach (see Figs. S19 and S20) is repeated for molecule 3, and Figs. S25 and S26 show the transmission coefficient curves of the four-square faces (four grey and two black curves), and eight hexagon faces (orange and grey curves). Remarkably, the transmission coefficients of bilayer **3**, present an opposite trend to bilayer **2**. In other words, the square faces are more sensitive than the hexagon ones. However, in general it appears that bilayer **2** yields larger conductance variations both for square and hexagonal faces.
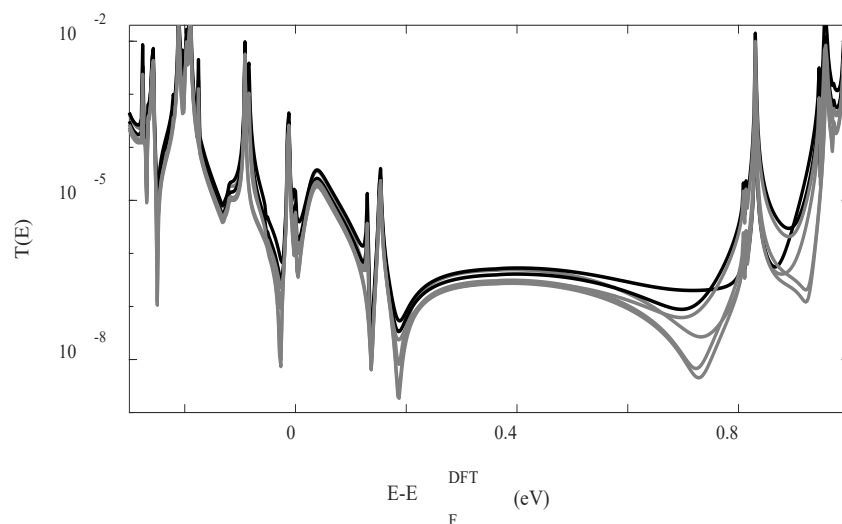
Figure S25: Zero-bias transmission coefficient $T(E)$ of Au-**3-PbS**-SLG junctions *vs* electron energy E. The bilayer (**3** + PbS) is formed where the molecule **3** bilayer connects to the quantum dot via square faces: grey curves are for pure Pb atoms at the surface while black curves are for a mixture of S and Pb atoms.
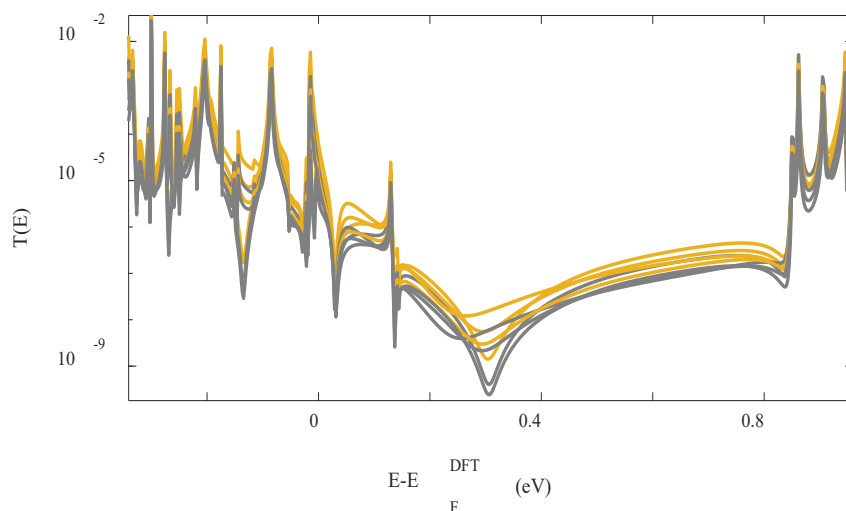

Figure S26: Zero-bias transmission coefficient $T(E)$ curves of Au-**3-PbS**-SLG junctions *vs* electron energy E. The bilayer (**3** + PbS) is formed where the molecule **3** bilayer connects to the quantum dot via hexagonal faces: orange curves are where the molecule attaches to S atoms at the surface while grey curves are for attachment to Pb atoms.

1.7 Transport through Au-molecule-SLG Junctions (in the absence of quantum dots)

In section 1.6, we explored transport through Au-molecule-dot-SLG junctions. To elucidate the effect of the quantum dot, we repeat the same simulations, but without the PbS quantum dot.
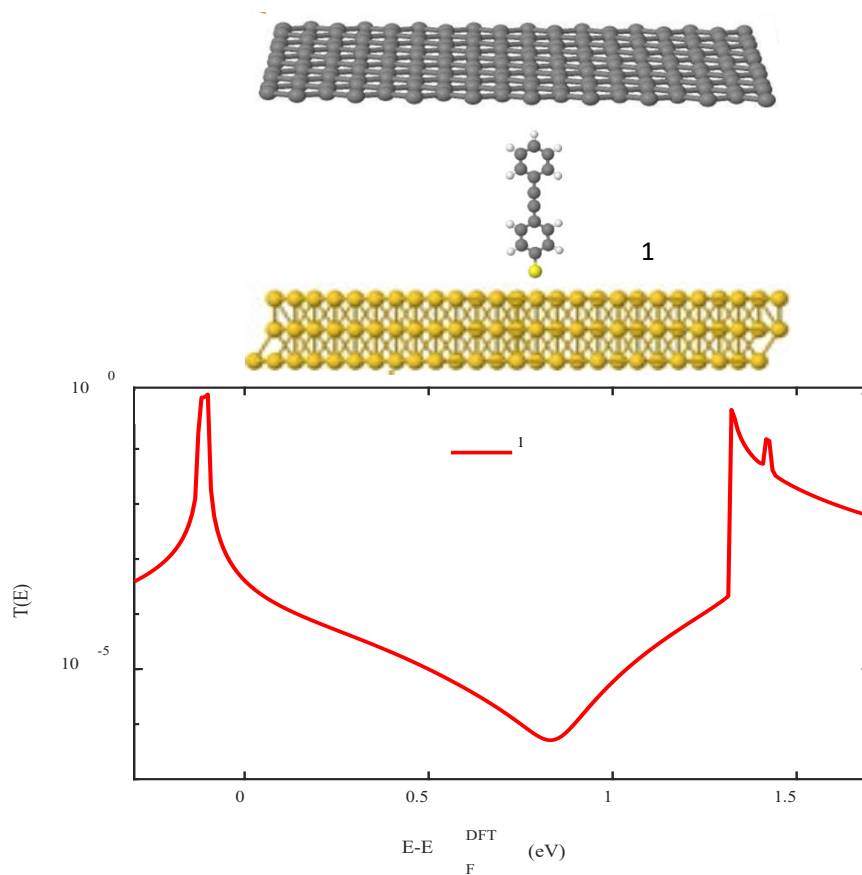
1.7.1 Au-1-SLG Junction

Figure S27: Top panel: Schematic illustration of the Au-**1**-SLG junction. Top contact is SLG and bottom contact is Au. Lower panel: Zero-bias transmission coefficient $T(E)$ for Au-**1**-SLG junction (The same as Fig. S18 as the quantum dot there had been washed away.)
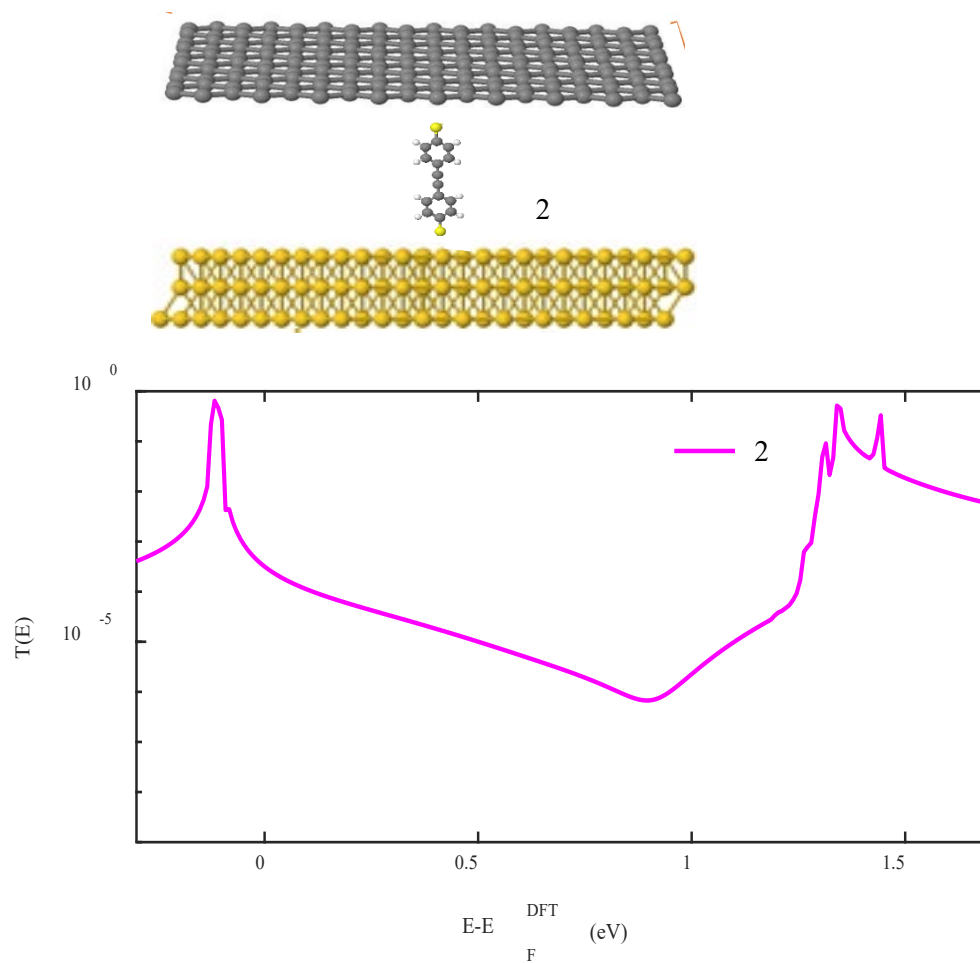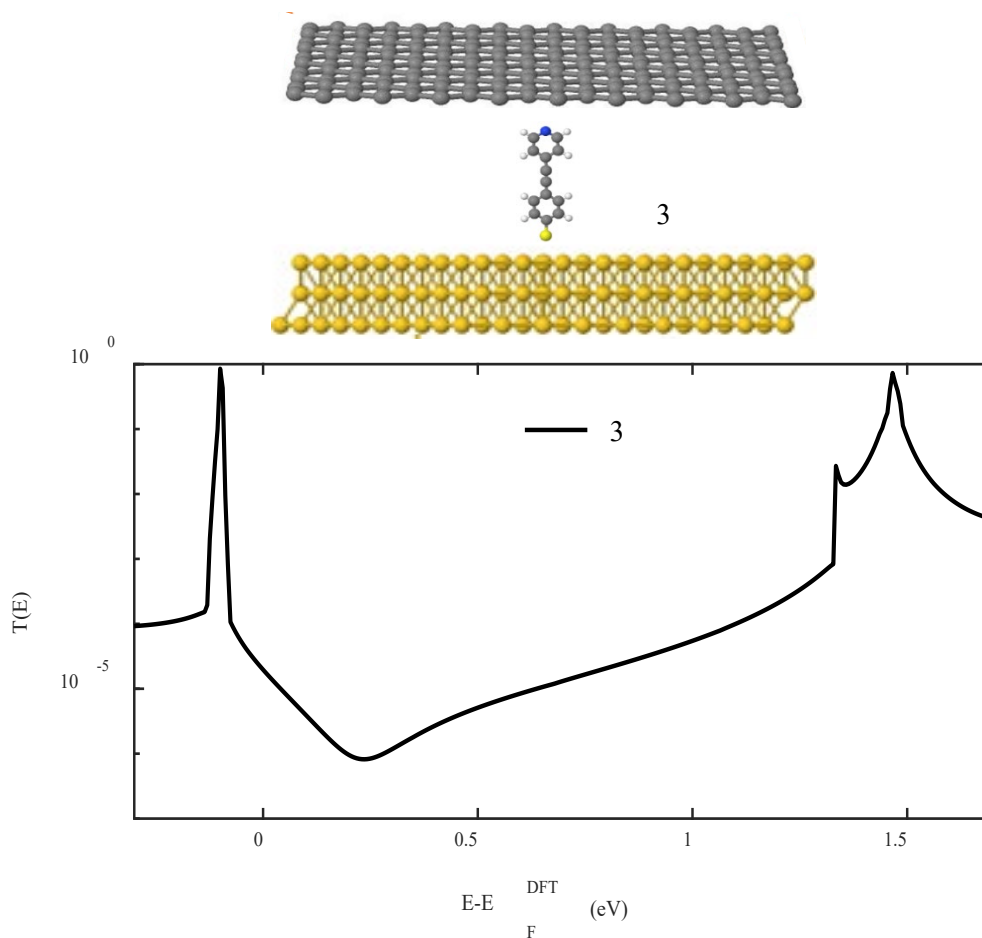
1.7.2 Au-2-SLG Junction

Figure S28: Top panel: Schematic illustration of the Au-**2**-SLG junction. Top contact is SLG and bottom contact is Au. Lower panel: Zero-bias transmission coefficient $T(E)$ for Au-**2**-SLG junction.

1.7.3 Au-3-SLG Junction

Figure S29: Top panel: Schematic illustration of the Au-**3**-SLG junction. Top contact is SLG and bottom contact is Au. Lower panel: Zero-bias transmission coefficient $T(E)$ for Au-**3**-SLG junction.

2. Experimental

2.1 Device Fabrication

The device fabrication procedure similar to our previously reported method.[9] The micro-well samples were fabricated on p-doped silicon wafers with a layer of 300 nm native wet-thermal silicon oxide. A standard cleaning method was applied to clean the surface before any photolithography process. The cleaning procedure starts with 5-minute immersion in acetone followed by a 2-minute immersion in propan-2-ol (IPA) to remove acetone residue.

The first photolithography step deposited gold fingers in the central area. A double-layer resist was used to achieve clean lift-off and precise edges. The bottom layer was formed by spinning LOR 5B (7000 rpm, 60 s) and the top layer was formed by spinning positive Shipley 1805 photoresist (S1805, 5500rpm, 60 s). Directly after coating with LOR 5B the sample was soft-baked for 10 minutes at 180°C to stabilise the film and improve the adhesion. After spinning the S1805, the samples were baked at 110°C for 2 minutes. The UV exposure time was 7.5 s; afterwards, the sample was developed in MICROPOSIT MF-319 developer for 20 s and then rinsed in DI water. Once the finger pattern had been developed, 5 nm titanium and 20 nm gold were evaporated onto the surface. SVC-14 positive photoresist stripper was used to lift off the unwanted metal.

A series of micro-wells was formed on top of the fingers by selectively etching holes in a 25 nm layer of aluminium oxide. First, atomic-layer deposition was used to deposit a high-quality layer of aluminium oxide with a precise thickness. Using photolithography, holes were opened up in the resist and buffered hydrofluoric acid was then used to etch through the aluminium oxide below, stopping at

the gold. Once the micro-wells were formed, S1805 was spun on, to protect the common contacts and gate electrode, and it was removed over the micro-well region using photolithography to allow molecule growth on the unprotected gold.

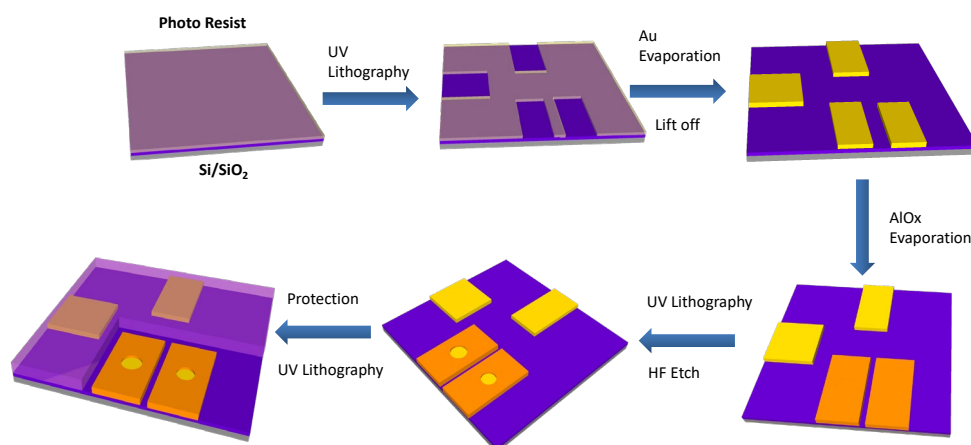A flow chart of device fabrication is shown in Figure S30.

Figure S30: Flow chart of micro-well device fabrication.

Each device after fabrication was washed with DI water (resistance > 10 MΩ) several times to eliminate any possible metal/salt contaminants, then immersed in hot dimethylformamide (DMF, Sigma-Aldrich, 99.8%, 90°C) for 20 minutes to wash off organic contaminants. The device after washing was rinsed successively in acetone, ethanol and IPA several times, and finally rinsed in DMF before put into the chosen solution of molecules to form a SAM.

2.2 QDs Synthesis and Characterization:

Colloidal lead sulfide (PbS) nanocrystals capped with oleic acid were synthesized by modifying a previously reported method[10]. Briefly, 5.6 mmol of lead oxide (PbO, 99.999%, Alfa Aesar) and 12.6 mmol of oleic acid (90%, Sigma Aldrich) were added to a three-necked round-bottom flask. The flask was then heated to 110 °C under vacuum ($< 10^{-2}$ mbar). After degassing, 25 mL of 1-octadecene (ODE, 90%, Sigma Aldrich) was injected into the flask while vigorously stirring the lead oleate solution. The mixture was maintained at 110 °C for 2 hours, yielding a colorless solution. Subsequently, the reaction flask was flushed with nitrogen and heated to 115 °C. Upon reaching 115 °C, a solution of hexamethyldisilathiane in ODE was rapidly injected into the lead precursor solution. The reaction mixture was then allowed to cool naturally to 60 °C and transferred to an argon-filled glovebox. To isolate the PbS nanocrystals, ethanol/butanol was added to the reaction mixture, followed by centrifugation at 12,000g. The precipitated nanocrystals were redispersed in toluene, and the precipitation/redispersion cycle was repeated multiple times to remove residual reaction solvents. The purified PbS nanocrystals were stored in a nitrogen-filled glovebox at a concentration of 20 mg/mL.

Atomic force microscopy (AFM) in tapping mode was used to characterize the size of quantum dots. Figure S31 (a) shows the synthesized QDs diluted to 2 mg/mL and spin-coated (500rpm for 30 seconds and 2000 rpm for 1 minutes) onto a template-stripped gold substrate (Au^{TS}) with a roughness of less than 100 pm . As the convolution factor typically leads to an overestimation of QD size, the height of the QDs on the Au^{TS} was used to estimate the actual QD size in this work. In total height of 100 QDs was measured, and the averaged size of QDs was estimated to be about 3.9 ± 0.5 nm (Figure S31 (b)). Considering the protection Oleic acid with chain length of 1nm on both sides, the size of QDs was estimated to be 1.9 ± 0.5 nm.
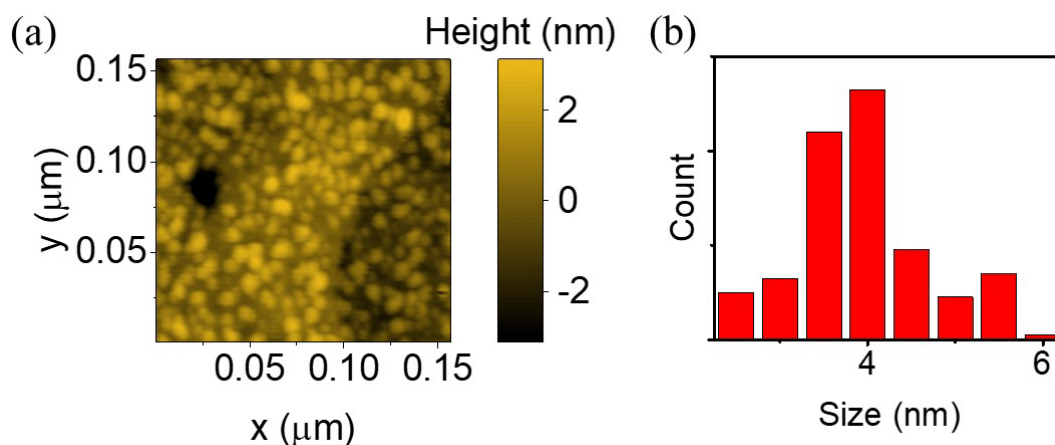
Figure S31: (a) AFM image of synthesized quantum dots deposited on template stripped gold substrate. (b) The size (height) distribution of quantum dots.

Beyond AFM, the size of QDs was also characterized by photoluminescence. Figure S32 (a) was the absorption and PL spectra of QDs solution, with intensity in arbitrary unit. The maximum PL wavelength was observed to be 840nm, which corresponding to a band gap (E_g) with energy of 1.48 eV. The QDs diameter, d, can be estimated via empirical equation reported previously[11]:

$$E_g = 0.41 + \frac{1}{0.0252d^2 + 0.283d}$$

The size distribution was then estimated to be 2.2 ± 0.3 nm. This result is comparable with the result measured via AFM technique (Figure S32 (b)), which confirmed the QDs size is about 2nm.
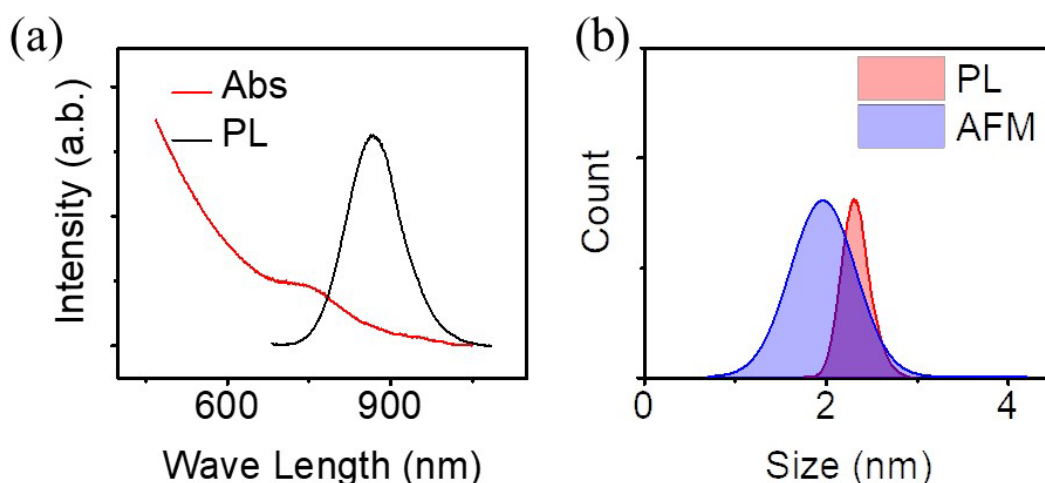

Figure S32: (a) Absorption and PL spectra of QDs synthesized. (b) Size distribution of QDs, estimated via AFM and PL measurement.

2.3 SAM and QD Growth

We used a modified standard method for SAM growth. The solution of molecules was prepared by dissolving target molecules in DMF with a concentration of 1 mM, and the solution was ultra-sonicated for 10 minutes to dissolve the molecules completely. The device after pre-treatment was immersed in

this solution for 30 minutes, washed with DMF, ethanol (EtOH), and IPA several times and re-immersed in the solution. This process was repeated several times, and after that, the device was immersed in the solution for 24−48 hours for SAM growth and self-organisation. Experiments suggest that this type of 'stepwise' self-assembly helps the SAMs to cure the pinholes and decrease the possibility of short circuits. The device after SAM growth was rinsed with DMF, ethanol and IPA several times to eliminate physisorbed molecules, and dried at 30°C.

The PbS nanocrystals capped with oleic acid were synthesized following the method in previous paper.[12] They were initially suspended in toluene with 20 mg/ml concentration, which were later diluted to 1 mg/ml for the QDs growth. The recipe for the nanocrystal deposition is based on our previous reported work.[12] After SAMs growth, the sample was immersed in the diluted solution for 24 hours. After immersion the sample was spin-coated with clean toluene to wash off the physiosorbed quantum dots. The spin-coating process was threefold. Firstly, we dispensed clean toluene (i.e., without suspending quantum dots) to cover the whole surface of the sample while the sample stayed static. Afterwards, it was spun at a low rate of 500 rpm/min for 10 s followed by a high rate of 2000 rpm/min for 20 s. This process was repeated 4 times to remove physiosorbed quantum dots. The detailed procedure is illustrated as Fig. S31.
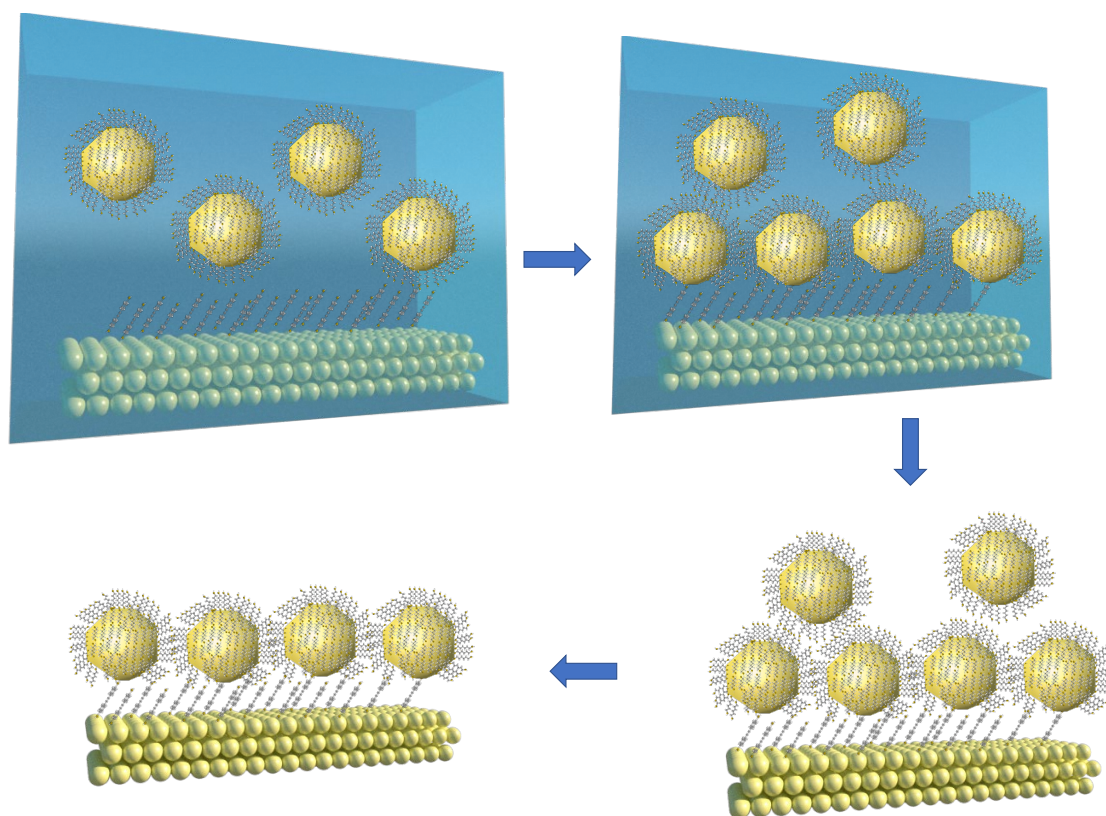

Figure S33: Assembly procedure of PbS quantum dots on molecular self-assembled monolayers, as described in section 2.2.

2.4 Graphene transfer

We followed the standard wet-transfer method to deposit the graphene layers.[13] Single-layered graphene on copper (Graphene supermarket, Graphene on 1 side) was used in this work. The copper etching procedure follows the standard recipe for graphene transfer.

0.1M ammonium persulfate (APS) was dissolved in water as the etchant solution. 4% PMMA was spin-coated on copper with graphene (6000rpm, 1min) as a protection layer, and incubated at 150°C for 1 minute to evaporate the solvent. After heating, PMMA/graphene/Cu was transferred into etchant solution for Cu etching. The etching process takes 18−24 hours. After copper etching, the graphene was

transferred into clean DI water 6 times, to wash off remaining APS, and the PMMA-protected graphene was transferred onto our device with SAM by 'fishing'.

Devices after graphene transfer were incubated at high vacuum (10^{-7} mbar) for 24 hours to evaporate any water. After drying, the PMMA was washed off by immersing the device in acetone, and rinsing it inside the acetone gently with a glass pipette. This procedure was repeated several times, and devices after rinsing were immersed in acetone overnight to eliminate PMMA residue. Figure S32 shows a flow chart for the graphene transfer.
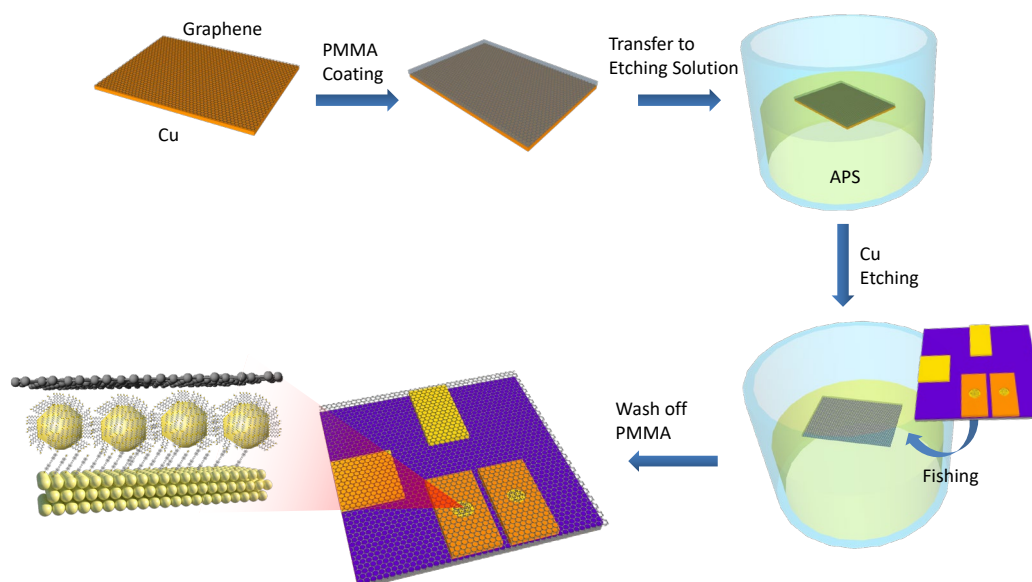
Figure S34: Flow chart of transfer of graphene on to a micro-well device**.**

2.5 Graphene patterning

The graphene was patterned in the same way as we previously reported.[9] Devices after PMMA removal were coated with S1805 photoresist by spin-coating, and dried in high vacuum overnight. UV lithography was used to pattern graphene strips on the micro-wells, and the unprotected graphene was removed with an RF plasma asher to separate the various wells.

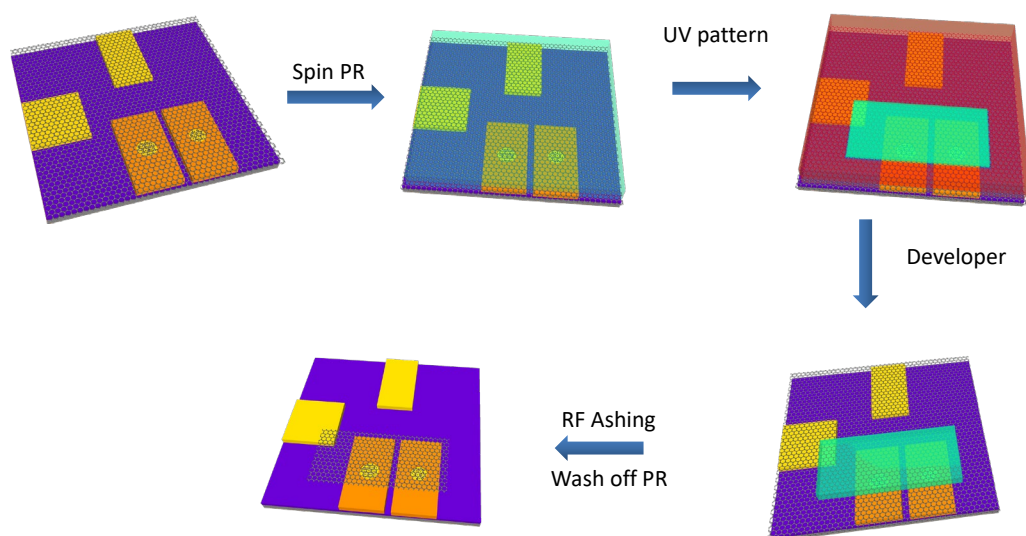The flow chart in Figure S33 shows these steps.

Figure S35: Flow chart of etching off unwanted graphene parts.

2.6 AFM Characterisation

AFM characterization was operated by MFP-3D AFM System (Asylum/Oxford Instruments). The topography of all the images was obtained by using a Multi75-G tip from Budget Sensors in tapping mode. For our devices, the roughness of the gold surface is larger than 1.5 nm, so it is hard to observe the quantum dot on the substrate. For this reason, we have also grown quantum dots on template-stripped gold (Au^{TS}, roughness < 0.1 nm) by the same method, and used AFM to characterize the QD assembly. Figure S34 shows Au^{TS}, Au^{TS} after SAM growth and Au^{TS} after QD assembly. Closely packed quantum dots on the substrate surface can be clearly seen. Figure S35 shows the size distribution of QDs assembled on the Au^{TS} surface. From this histogram, the average QD size is 6.1±1.2 nm. Considering that the diameter of a QD is 2 nm, so that the total size is 2 nm (length of oleic acid) + 2 nm (QD diameter) + 2 nm (length of oleic acid) ≈ 6nm, the size distribution obtained from AFM characterization is comparable.
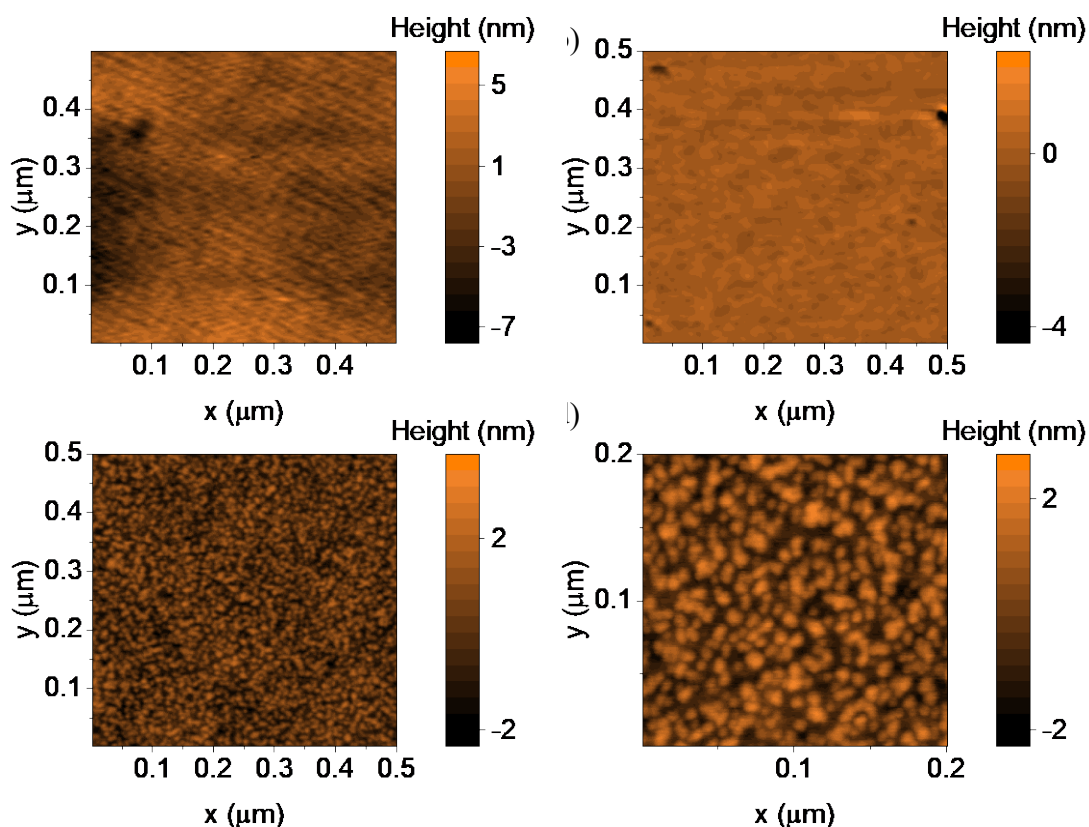

Figure S36: AFM image of a clean Au^{TS} (a), Au^{TS} after SAM growth (b), and Au^{TS}/SAM after QD growth at large (500 nm, c) and small (200 nm, d) scales.
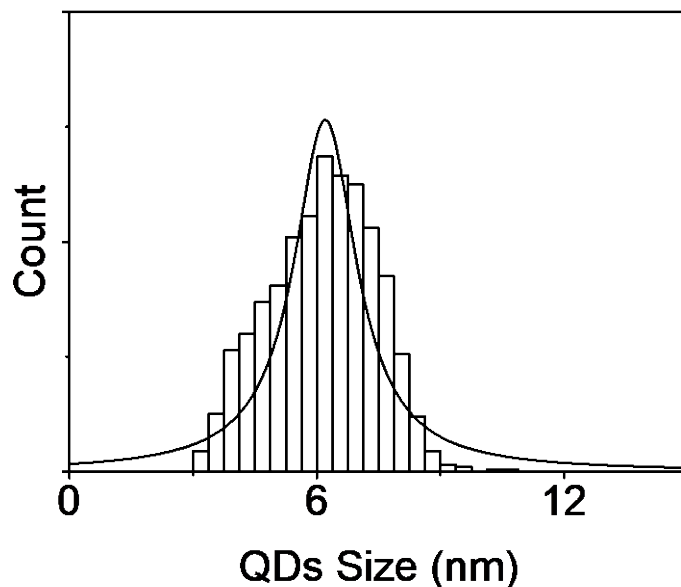
Figure S37 Size distribution of QDs assembled on Au-SAM surface. The distribution obtained from counting 200 QDs on 10 random spots.

2.7 Electrical Measurement

Each device after fabrication was wire-bonded to a leadless chip carrier, keeping the temperature below 35°C. The DC bias voltage between source and drain (V_{SD}) was generated using a Keithley 2400 SMU (floating) and added to the AC voltage generated from an SR830 lockin amplifier (10 mV amplitude, 127 Hz frequency) using a homemade DC/AC mixer. A Femto DLPCA 200 current pre-amplifier was used to amplify the alternating current before it as measured by the lockin amplifier to provide the differential conductance ($\mathrm{d}I/\mathrm{d}V_{SD}$). The SMU measured the direct current I.

For each type of molecule, at least two independent batches of samples were prepared (with the same recipe) to prove reproducibility and detect unwanted one-off effects (contamination, low-quality graphene, bad SAM, etc.). If data showed signs of bad SAM or graphene quality (many shorts or low Au/graphene/Au conductance), or the measured conductances had a large disagreement with each other, more batches were prepared and measured.
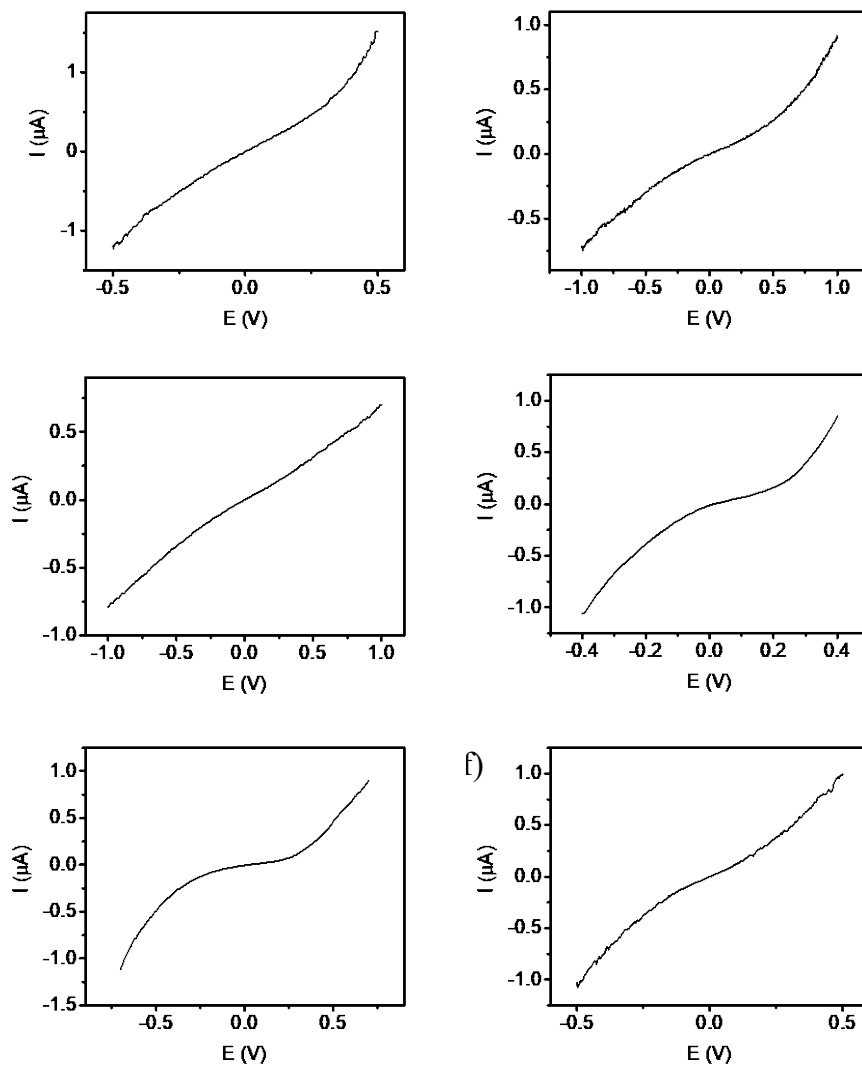
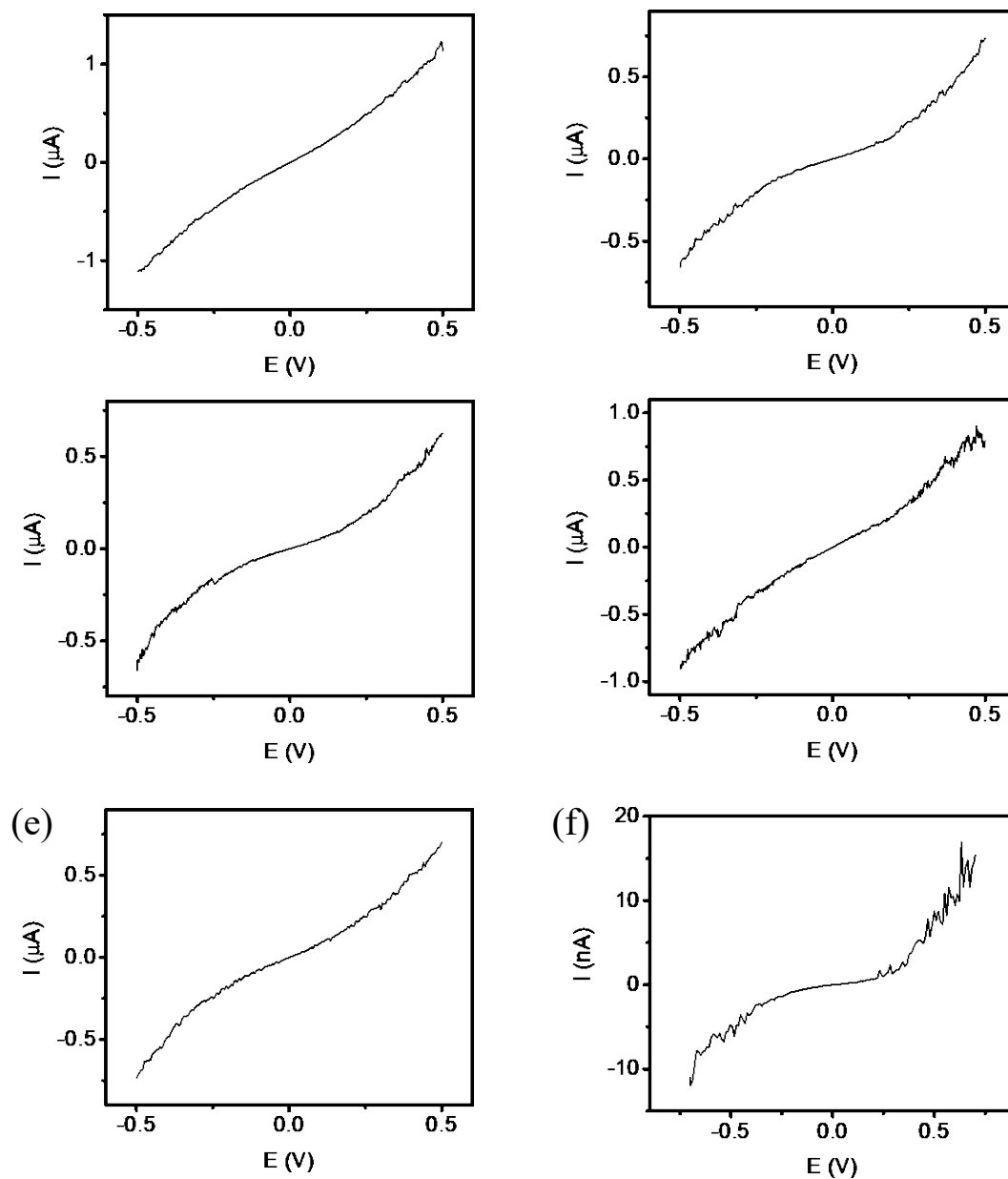**Figure S38:** IV curves for SAM**1** device without QD growth.

Figure S39: IV curves for SAM**1** device with QD growth.

Figures S36 and S37 show the IV curves from device of SAM**1** with and without QD growth, respectively. The IV curves are a similar shape, which indicates that the QDs do not grow well on SAM**1**.
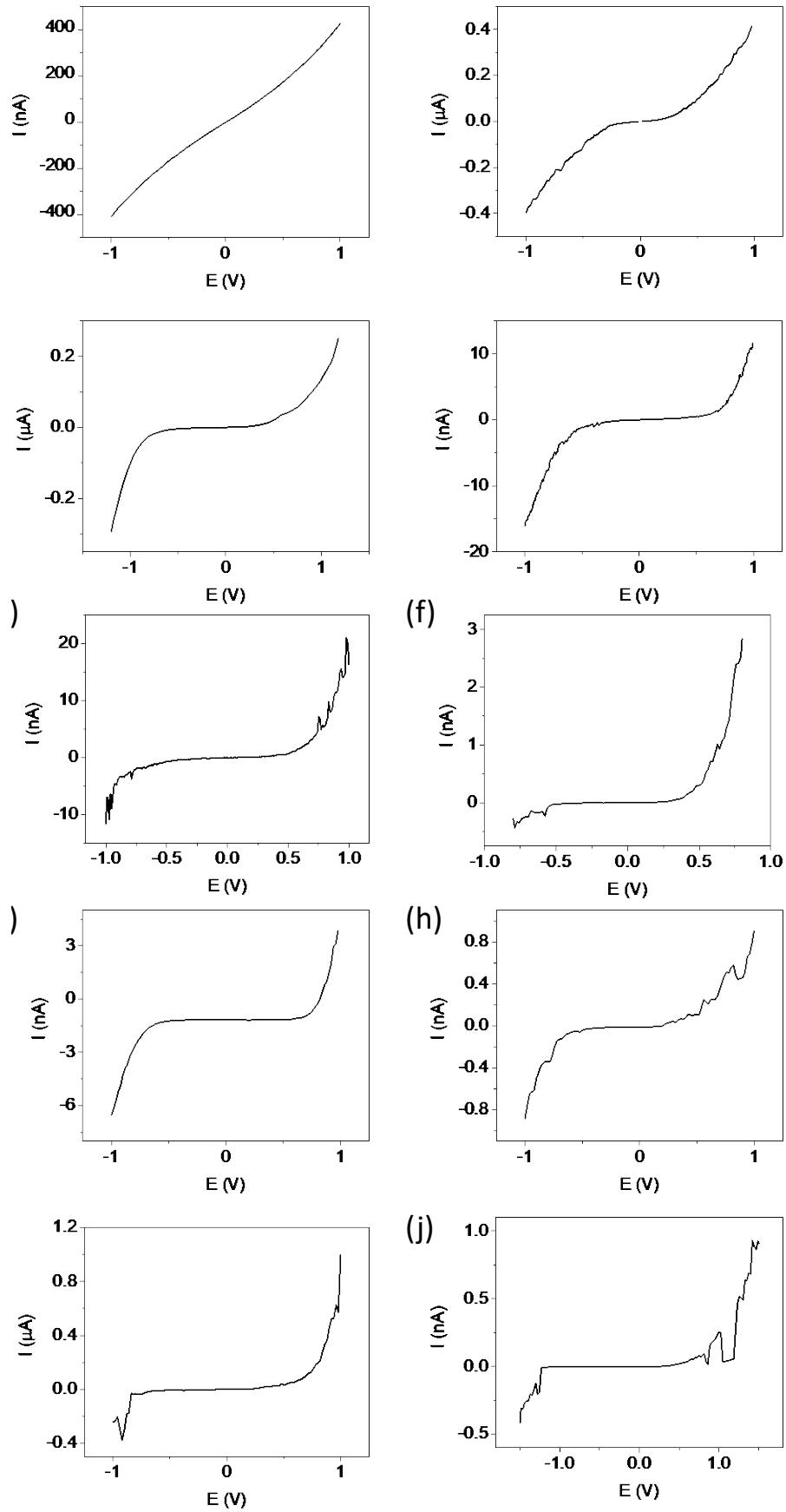
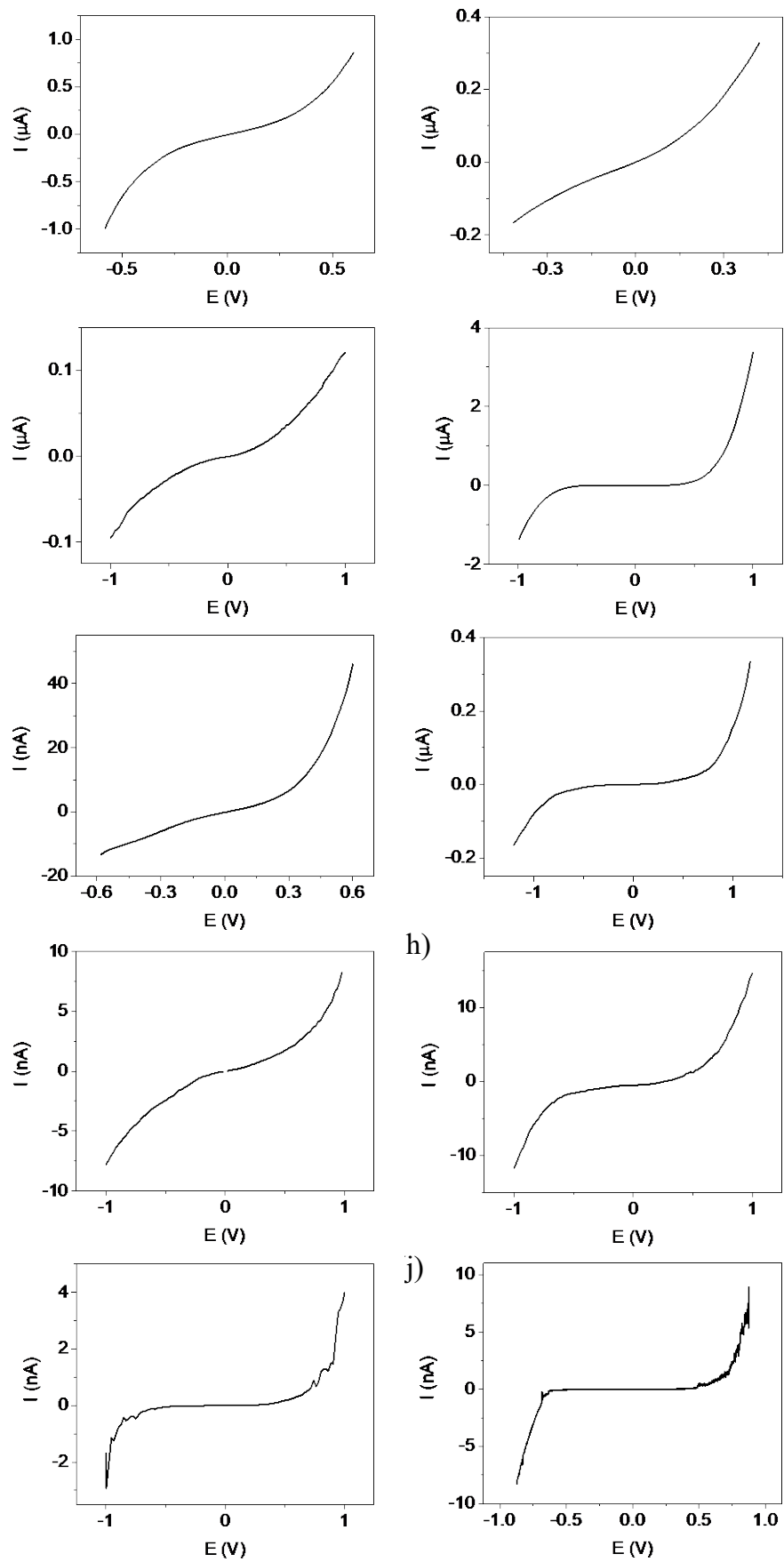**Figure S40:** IV curves for SAM**2** device with QD growth.

Figure S41: IV curves for SAM**3** device with QD growth.

2.8 Room-temperature electrostatic-gate investigation

We use ionic liquid to investigate the behaviour of Au-SAM-QDs-Graphene junctions. The measurement is at room temperature—for the measurement details, refer to our previous work on Au-SAM-Graphene junctions.[9]

A small droplet of ionic liquid (DEME-TFSI, Sigma Aldrich, >98.5%, ~50 μL) was dropped on to the device. The device was checked in an optical microscope to ensure that all the micro-wells and gate electrodes were covered by the ionic liquid. A gate voltage was applied between the gate electrode and the common drain electrode using a second Keithley 2400 SMU, keeping the gate voltage in the range where there was almost no leakage current. At each gate voltage, the ionic liquid was given 240 s to equilibrate, and then the SD voltage was applied and electrical transport was measured as described in section 2.6, above. I-V characteristics of the junction at zero gate voltage were measured before and after applying the series of gate voltages, and also compared with the I-V curve before addition of the ionic liquid, to ensure that the ionic liquid and gate voltage did not destroy the junction.
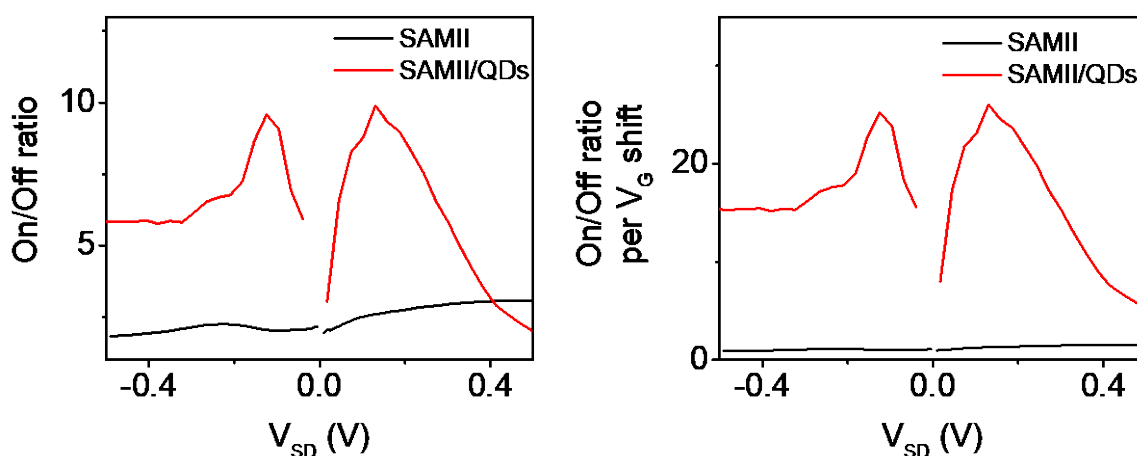
Figures S40−S45 show various

Figure S42 (Left) On/off ratio for Au/SAM**2**/Graphene and Au/SAM**2**/QDs/Graphene. (Right) same as left but scaled by the shift in gate voltage between On and Off states.
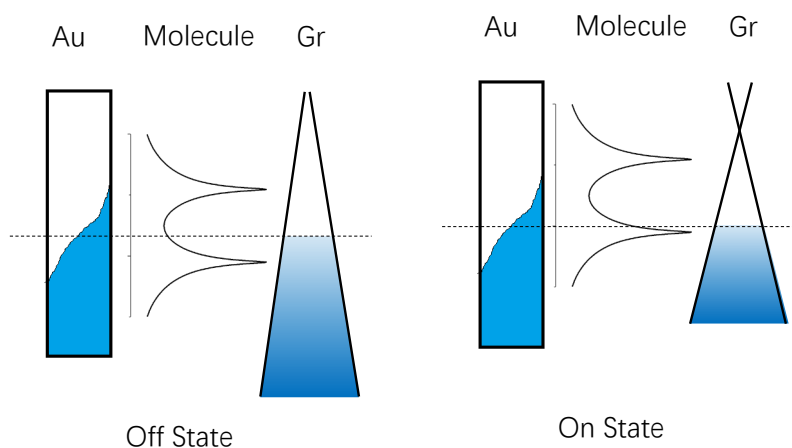

Figure S43 (Left) Energy diagram for Au/SAM/Graphene junction in Off and On states, taking the graphene to be doped p-type.
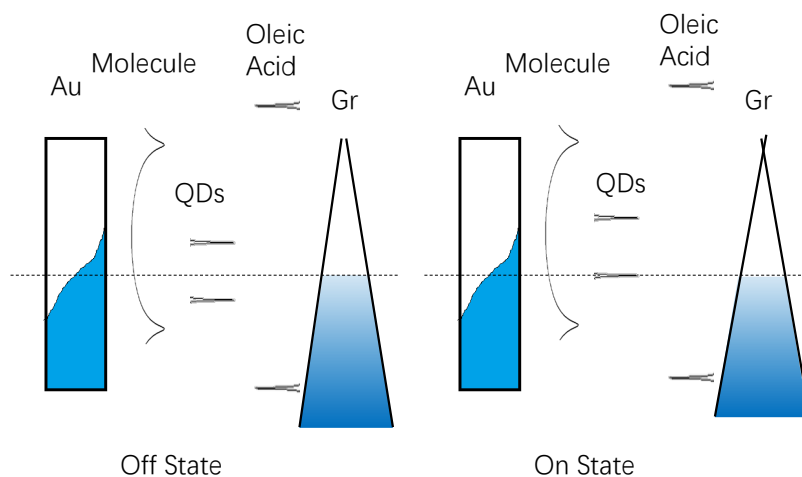
Figure S44 (Left) Energy diagram for Au/SAM/QDs/Graphene junction in Off and On states.
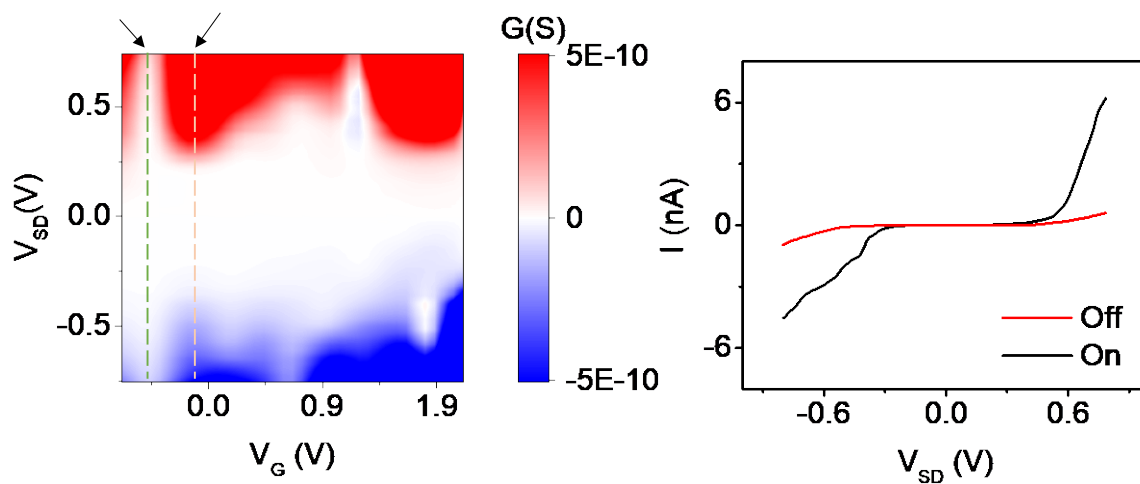

Figure S45 (Left) Plot of measured current vs. gate voltage vs. source/drain voltage of Au/SAM**3**/QDs/Gr junction. The dashed line corresponds to a high-current (on) and low-current (off) state at different gate voltages. (Right) IV curve of Au/SAM**3**/QDs/Gr junction in the On and Off states.
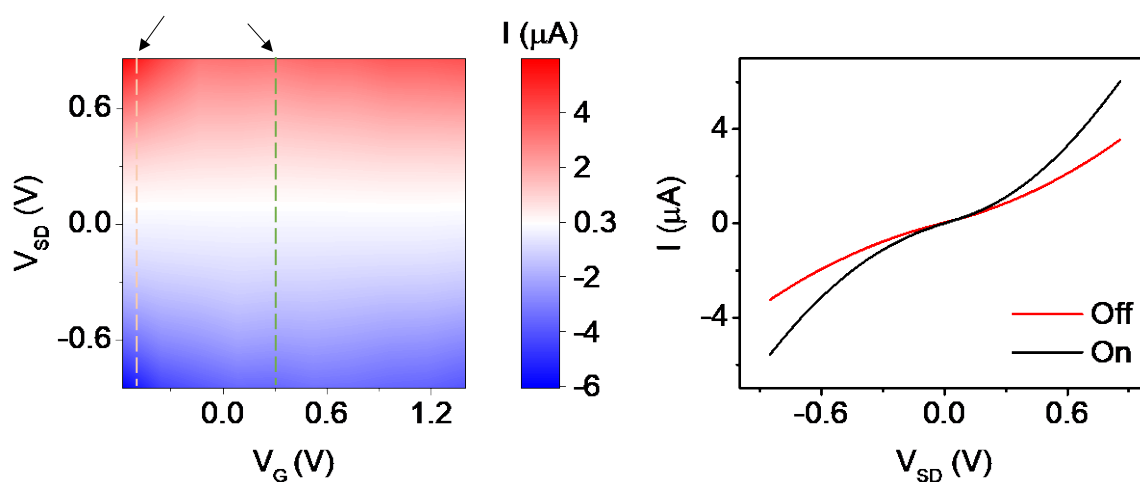
Figure S46: (Left) Plot of measured current vs. gate voltage vs. source/drain voltage of Au/SAM**3**/Gr junction. The dashed lines correspond to high-current (on) and low-current (off) states. (Right) IV curve of Au/SAM**3**/QDs/Gr junction in the On and Off states.
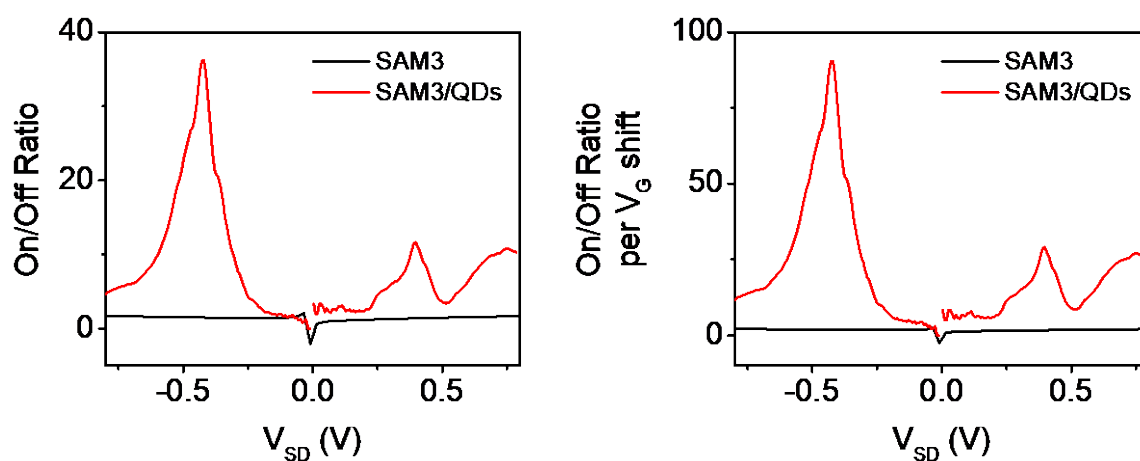

Figure S47: (Left) On/off ratio for Au/SAM**3**/Graphene and Au/SAM**3**/QDs/Graphene. (Right) Same as left but scaled by the shift in gate voltage between On and Off states.
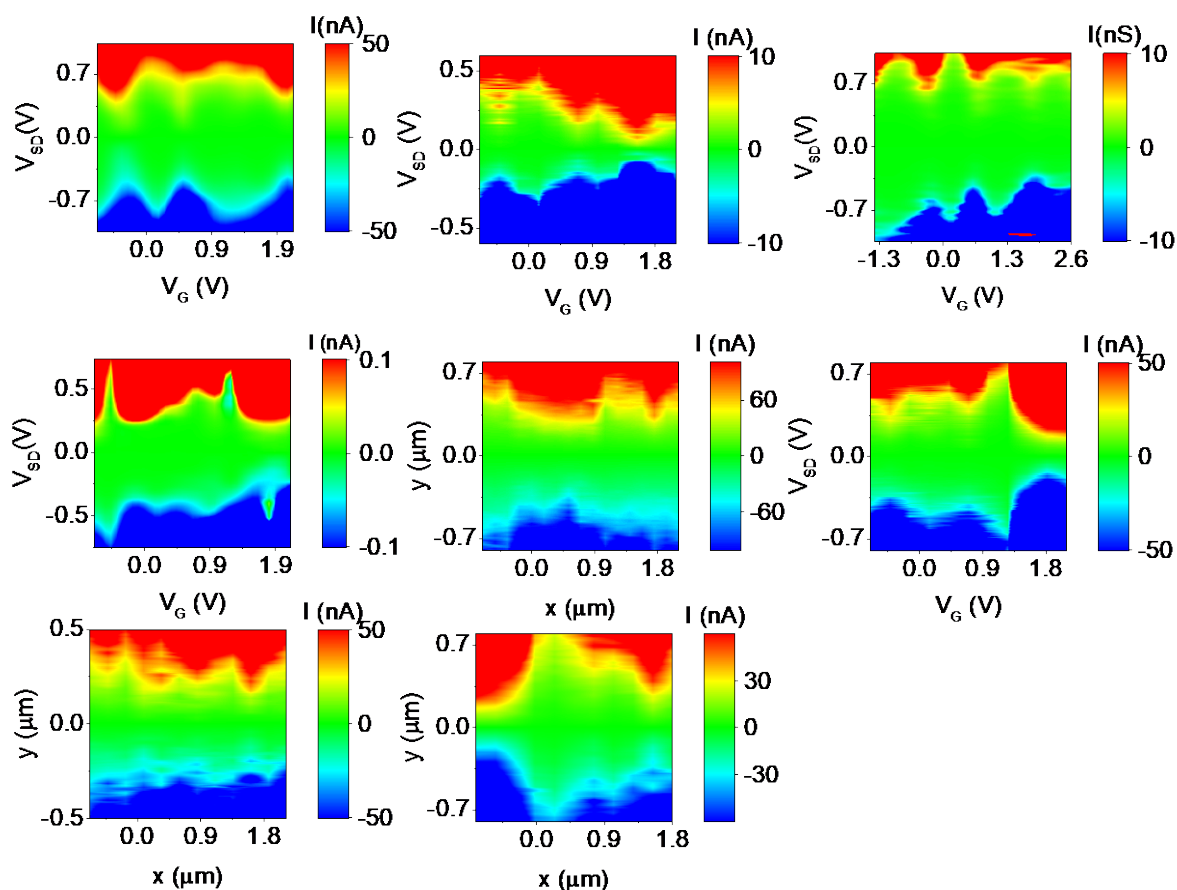
Figure S48: Collection of measured current vs. gate voltage vs. source/drain voltage for measured by layer junctions, (a-c) molecule 2+QDs, (d-h) molecule 3 + QDs.

References

1.   Soler, J. M.; Artacho, E.; Gale, J. D.; García, A.; Junquera, J.; Ordejón, P.; Sánchez-Portal, D. J. J. o. P. C. M., The SIESTA method for ab initio order-N materials simulation. *Journal of Physics: Condensed Matter* 2002, *14* (11), 2745.

2.   Perdew, J. P.; Burke, K.; Ernzerhof, M., Generalized gradient approximation made simple. *Physical Review Letters* 1996, *77* (18), 3865.

3.   Becke, A. D., Density-functional exchange-energy approximation with correct asymptotic behavior. *Physical review A* 1988, *38* (6), 3098.

4.   Perdew, J. P.; Wang, Y., Accurate and simple analytic representation of the electron-gas correlation energy. *Physical review B* 1992, *45* (23), 13244.

5.   Giansante, C.; Infante, I., Surface traps in colloidal quantum dots: a combined experimental and theoretical perspective. *The journal of physical chemistry letters* 2017, *8* (20), 5209-5215.

6.   Kobko, N.; Dannenberg, J., Effect of basis set superposition error (BSSE) upon ab initio calculations of organic transition states. *The Journal of Physical Chemistry A* 2001, *105* (10), 1944-1950.

7.   Sherrill, C. D., Counterpoise correction and basis set superposition error. *School of Chemistry and Biochemistry, Georgia Institute of Technology* 2010.

8.   Sinnokrot, M. O.; Valeev, E. F.; Sherrill, C. D., Estimates of the ab initio limit for $\pi-\pi$ interactions: The benzene dimer. *Journal of the American Chemical Society* 2002, *124* (36), 10887-10893.

9.   Wang, X.; Ismael, A.; Ning, S.; Althobaiti, H.; Al-Jobory, A.; Girovsky, J.; Astier, H. P.; O'Driscoll, L. J.; Bryce, M. R.; Lambert, C. J., Electrostatic Fermi level tuning in large-scale self-assembled monolayers of oligo (phenylene–ethynylene) derivatives. *Nanoscale Horizons* 2022, *7*, 1201-1209.

10.   Davis, N. J. L. K.; Allardice, J. R.; Xiao, J.; Karani, A.; Jellicoe, T. C.; Rao, A.; Greenham, N. C., Improving the photoluminescence quantum yields of quantum dot films through a donor/acceptor system for near-IR LEDs. *Mater Horiz* **2019,** *6* (1), 137-143.

11.   Moreels, I.; Lambert, K.; Smeets, D.; De Muynck, D.; Nollet, T.; Martins, J. C.; Vanhaecke, F.; Vantomme, A.; Delerue, C.; Allan, G., Size-dependent optical properties of colloidal PbS quantum dots. *ACS nano* **2009,** *3* (10), 3023-3030.

12.   Fruhman, J. M.; Astier, H. P.; Ehrler, B.; Böhm, M. L.; Eyre, L. F.; Kidambi, P. R.; Sassi, U.; De Fazio, D.; Griffiths, J. P.; Robson, A. J., High-yield parallel fabrication of quantum-dot monolayer single-electron devices displaying Coulomb staircase, contacted by graphene. *Nature Communications* 2021, *12* (1), 4307.

13.   Bae, S.; Kim, H.; Lee, Y.; Xu, X.; Park, J.-S.; Zheng, Y.; Balakrishnan, J.; Lei, T.; Ri Kim, H.; Song, Y. I., Roll-to-roll production of 30-inch graphene films for transparent electrodes. *Nature nanotechnology* 2010, *5* (8), 574-578.